1995ApJ...445..433A

THE ASTROPHYSICAL JOURNAL, 445:433–450, 1995 May 20
© 1995. The American Astronomical Society. All rights reserved. Printed in U.S.A.

MODEL ATMOSPHERES FOR M (SUB)DWARF STARS. I. THE BASE MODEL GRID

FRANCE ALLARD
Department of Geophysics and Astronomy, University of British Columbia, Vancouver, B.C., Canada V6T 1Z4;
allard@astro.ubc.ca

AND

PETER H. HAUSCHILDT
Department of Physics and Astronomy, Arizona State University, Box 871504, Temple, AZ 85287-1504:
yeti@sara.la.asu.edu

Received 1994 August 10; accepted 1994 November 22

ABSTRACT

We have calculated a grid of more than 700 model atmospheres valid for a wide range of parameters encompassing the coolest known M dwarfs, M subdwarfs, and brown dwarf candidates: $1500 \leq T_{\rm eff} \leq 4000$ K, $3.5 \leq \log g \leq 5.5$, and $-4.0 \leq [M/{\rm H}] \leq +0.5$.

Our equation of state includes 105 molecules and up to 27 ionization stages of 39 elements. In the calculations of the base grid of model atmospheres presented here, we include over 300 molecular bands of four molecules (TiO, VO, CaH, FeH) in the JOLA approximation, the water opacity of Ludwig (1971), collision-induced opacities, *b–f* and *f–f* atomic processes, as well as about 2 million spectral lines selected from a list with more than 42 million atomic and 24 million molecular (H_2, CH, NH, OH, MgH, SiH, C_2, CN, CO, SiO) lines. High-resolution synthetic spectra are obtained using an opacity sampling method. The model atmospheres and spectra are calculated with the generalized stellar atmosphere code PHOENIX, assuming LTE, plane-parallel geometry, energy (radiative plus convective) conservation, and hydrostatic equilibrium.

The model spectra give close agreement with observations of M dwarfs across a wide spectral range from the blue to the near-IR, with one notable exception: the fit to the water bands. We discuss several practical applications of our model grid, e.g., broadband colors derived from the synthetic spectra. In light of current efforts to identify genuine brown dwarfs, we also show how low-resolution spectra of cool dwarfs vary with surface gravity, and how the high-resolution line profile of the Li I resonance doublet depends on the Li abundance.

Subject headings: atomic data — molecular data — stars: atmospheres — stars: late-type — subdwarfs

1. INTRODUCTION

Interest in the extreme lower main sequence has blossomed in recent years, largely because of its implications for star formation theory and dark matter candidates. Advances in spectroscopy and photometry, especially at infrared wavelengths, promise a wealth of new data on low-mass stars. Therefore, parallel improvements in models of cool stellar atmospheres are very important if the full potential of these data is to be realized.

The lower main sequence is populated by a variety of objects—old disk M dwarfs, halo population subdwarfs, and possibly even young, still contracting brown dwarfs. The proper detection and classification of these objects requires synthetic spectra which can quantify their basic properties: elemental abundances, effective temperature, surface gravity, and (if the parallax is available) the radius, mass, and luminosity. At present, these physical properties are not yet particularly well determined. Traditional techniques to estimate stellar effective temperature based on blackbody approximations and broadband photometry are at best dangerous (and at worst, invalid) for cool M dwarfs, whose true continua are masked by extensive molecular absorption. Therefore, "observed" positions of these stars in the H-R diagram are highly uncertain. Such uncertainties can have profound implications for star formation theory and the search for brown dwarfs (Burrows & Liebert 1993).

The success of modeling atmospheres for low-mass stars relies heavily on the treatment and quality of the opacities. The first grid of model atmospheres of M dwarfs to include molecular and atomic line blanketing as well as convection by Mould (1976), based on his thesis, covered an effective temperature range from 4250 K down to 3000 K, whereas many of the faint well-observed stars have colors implying temperatures as much as 1200 K cooler (H. Jones private communication). Although Mould's models represented an important breakthrough to the lower main sequence, they nevertheless failed to reproduce key observed characteristics of M dwarfs even in the range of $T_{\rm eff}$ they covered.

Since the early computations of Mould, significant improvements to molecular and atomic data bases have been achieved, enabling the construction of model atmosphere grids for M dwarfs which can be compared directly to the coolest observed spectra. A new generation of model calculations, by Allard (1990) and Kui (1991), was able to reproduce many of the observed features found in the optical and near-IR. The first set of Allard model atmospheres were used by Kirkpatrick et al. (1993) to obtain an M dwarf temperature sequence which succeeded in bringing at least the hotter dM's close to the theoretical main sequence.

However, like Mould's models before them, these models disagreed with observations on several points. For example, they did not reproduce $I-J$ colors of dM stars, they could not match the IR flux distribution dominated by water band absorption, and significant problems remained in the UV and IR for the low-metallicity subdwarfs as well.

© American Astronomical Society • Provided by the NASA Astrophysics Data System

1995ApJ...445..433A

Allard (1994) has addressed and corrected several of these discrepancies in a test model of the spectral distribution of the classical dwarf VB 10. In this paper, we present an improved generation of models which incorporates the results of Allard (1994). We also include many more metal lines, which are critical for the energy balance and serve as important diagnostics of the synthetic spectra. The number of molecules in both the equation of state (EOS) and the opacity calculations has been significantly increased compared to any previous calculations. Furthermore, we have extended our opacity sampling method to include up to 25 million molecular lines, which both replace older just overlapping line approximation (JOLA) band opacities and added new opacity sources. This new grid of cool dwarf atmospheres significantly improves upon the work of Allard (1990).

In the next section we present the most important aspects of the model construction and discuss the model grid and the effects of some model parameters on the model structure and on the resulting synthetic spectra in § 3. Finally we summarize the main properties of the new grid in § 3.3 by confronting it with observations in selected color-color planes.

2. MODEL CONSTRUCTION

Our model atmospheres are constructed under the classical assumptions of stellar atmosphere theory, implemented in our model atmosphere code PHOENIX, version 4.9. PHOENIX was first developed to treat the expanding ejecta of novae and supernovae; as a result, it is capable of solving the (special relativistic) radiative transfer equation (RTE) in the Lagrangian frame self-consistently with multilevel, non-LTE rate equations and the (special relativistic) radiative equilibrium (RE) equation in the Lagrangian frame. Numerical methods used in PHOENIX include the solution of (i) the RTE using the accelerated lambda iteration (ALI) method described by Hauschildt (1992) and Hauschildt et al. (1994b), and the (ii) multilevel non-LTE continuum and line transfer problem using the ALI algorithm (Hauschildt 1993). More details on these aspects of the code can be found in Hauschildt, Störzer, & Baron (1994b) and Baron, Hauschildt, & Branch (1994).

Important additions to PHOENIX were necessary to handle the problems specific to compact cool dwarf atmospheres. The most important modifications, many of which were adapted from Allard (1990, 1994), are (i) solution of the EOS simultaneously for more than 334 species including diatomic and polyatomic molecules, (ii) inclusion of van der Waals atomic line broadening, (iii) inclusion of molecular opacities in the JOLA as well as several pretabulated straight mean (SM) molecular opacities, (iv) inclusion of molecular lines for a number of molecules, (v) treatment of convection using the mixing length formalism, and (vi) solution of the RE equation by a modified Unsöld-Lucy method.

The model atmosphere problem (i.e., the self-consistent simultaneous solution of the EOS, the hydrostatic equation, the RTE at all wavelengths, the radiative-plus-convective energy equation, and the non-LTE multilevel transfer and rate equations) is treated using a nested iteration scheme like that described by Hauschildt (1991).

Not all aspects of cool dwarf stars lead to additional complications in the model calculations; some actually allow us simplifications that substantially reduce the CPU time required per model calculation. First, since their surface gravities are fairly high ($\log g > 3$) such that the atmospheres have a relative extension of less than 1%, we can safely treat those atmospheres using a plane-parallel and static approximation. We have performed test calculations with the spherically symmetric mode of PHOENIX for some models with $\log g = 3.0$ and found (as expected) no significant differences in the models and synthetic spectra compared to the plane-parallel case. Second, the velocities of the convective cells in these stars are too small to be detectable in the low-resolution spectra we wish to reproduce, and furthermore, have a negligible effect on the transfer of line radiation. Therefore, we follow Allard's (1990) approach and neglect the effects of convective motions on line formation. Finally, we neglect for simplicity possible departures from LTE and external radiation fields.

The model atmospheres are characterized by the following parameters: (i) the surface gravity, $\log g$, (ii) the effective temperature, $T_{\rm eff}$, (iii) the mixing length to scale height ratio, l, here taken to be unity, (iv) the isotropic microturbulent velocity, ξ, and (v) the element abundances, here parameterized by $[M/H]$, the logarithm of the metal abundance (by number) relative to the solar abundances (Anders & Grevesse 1989).

2.1. *Hydrostatic Equation and Optical Depth Grid*

PHOENIX uses a prescribed optical depth grid to perform the model calculations. This grid is defined at one chosen wavelength. For this paper, we take the "standard optical depth" $\tau_{\rm std}$ as the continuum optical depth in absorption at 1.2 μm. We use a logarithmic $\tau_{\rm std}$ grid. A representative grid typically contains 50 points between $\tau_{\rm std} = 10^{-10}$ and 10^{2}, which ensures good τ resolution for all wavelength points in the model. This is important since opacities in M dwarfs are extremely nongray due to the simultaneous presence of lines, bands, and continuum. This particular $\tau_{\rm std}$ grid was also chosen such as to assure both high accuracy and high performance of the ALI radiative transfer method used in PHOENIX.

To solve the hydrostatic equation,

$$\frac{dP}{dr} = -g\rho \, ,$$

where $P = P_g + P_r$ is the total (gas pressure P_g and radiative pressure P_r) pressure, r the radius, g the gravity, and ρ the density, we first introduce the standard optical depth $\tau_{\rm std}$ as a new independent variable via $d\tau_{\rm std} = -\chi_{\rm std}\, dr$, with the initial condition $\tau_{\rm std} = 0$ for $r = r_{\rm out}$. Hence, we obtain

$$\frac{dP}{d\tau_{\rm std}} = \frac{g\rho}{\chi_{\rm std}} \, .$$

At the beginning of each iteration, we integrate this equation numerically for the current run of the electron temperature $T_e(\tau_{\rm std})$ in the radiative zones and simultaneously with the adiabatic temperature gradient equation for the convective zones using a Bulirsch-Stoer numerical quadrature method with adaptive step size; see Allard (1990) for details of this procedure. For the conditions present in M dwarfs, the radiation pressure gradient as well as the gradient of the turbulent pressure are much smaller than the gas pressure in all models considered here, so that we can set $P = P_g$ without loss of accuracy.

2.2. *EOS and Adiabatic Gradient*

The EOS used in this work includes up to 26 ionization stages of 39 elements (H, He, Li, Be, B, C, N, O, F, Ne, Na, Mg, Al, Si, P, S, Cl, Ar, K, Ca, Sc, Ti, V, Cr, Mn, Fe, Co, Ni, Cu, Zn,

© American Astronomical Society • Provided by the NASA Astrophysics Data System

1995ApJ...445..433A

TABLE 1

MOST IMPORTANT SPECIES IN THE EOS

Element	Compounds
H.....	H^+, H, H^-, H_2, OH, CH, NH, MgH, CaH, SiH, HCl, HF, HS, FeH, H_2O, CaOH, HCN, C_2H_2, CH_2, CH_4, C_2H, NH_2, NaOH, MgOH, AlOH, H_2S, KOH, CH_3, C_3H, NH_3
He	He^+, He
Li	Li^+, Li, Li^-, LiCl, LiOH
Be.....	Be^+, Be
C.....	C^+, C, C^-, C_2, CH, CN, CO, CS, CO_2, HCN, C_2H_2, CH_2, CH_4, C_2H, C_3, SiC_2, CH_3, C_3H, C_2N_2, C_2N, Si_2C, CS_2, SiC
N.....	N^+, N, N_2, NH, CN, HCN, NH_2, NH_3, C_2N_2, C_2N
O.....	O^+, O, O^-, OH, CO, TiO, ZrO, VO, SiO, H_2O, CO_2, CaOH, AlOF, NaOH, MgOH, Al_2O, AlOH, SiO_2, KOH, TiO_2, VO_2, AlOCl
F.....	F^+, F, F^-, HF, AlF, CaF, AlOF, CaF_2, TiF_2
Na	Na^+, Na, NaCl, NaOH
Mg.....	Mg^+, Mg, MgH, MgOH
Al.....	Al^+, Al, AlF, AlCl, AlOF, Al_2O, AlOH, AlOCl
Si.....	Si^+, Si, Si^-, SiH, SiO, SiS, SiO_2, SiC_2, Si_2C, SiC
P.....	P^+, P
S.....	S^+, S, S^-, HS, SiS, CS, TiS, H_2S, CS_2
Cl.....	Cl^+, Cl, Cl^-, HCl, NaCl, AlCl, KCl, CaCl AlOCl, $CaCl_2$
K.....	K^+, K, KCl, KOH
Ca	Ca^+, Ca, Ca^-, CaH, CaF, CaCl, CaOH, CaF_2, $CaCl_2$
Sc.....	Sc^+, Sc
Ti.....	Ti^+, Ti, TiO, TiS, TiO_2, TiF_2
V.....	V^+, V, VO, VO_2
Cr.....	Cr^+, Cr
Mn.....	Mn^+, Mn
Fe.....	Fe^+, Fe, FeH, FeO
Ni.....	Ni^+, Ni
Cu	Cu^+, Cu
Sr	Sr^+, Sr
Y.....	Y^+, Y
Zr.....	Zr^+, Zr, ZrO
Ba.....	Ba^+, Ba

Ga, Kr, Rb, Sr, Y, Zr, Nb, Ba, and La) as well as 105 molecules (Allard 1990, 1994, see Table 1 for a list of the most important molecules). Although grains and dust may be of importance in the atmospheres of the coolest M dwarfs, they have not been included at this level of our calculations but are planned for future studies.

We assume particle and charge conservation in each layer of an ideal gas. Although PHOENIX generally accounts for non-LTE effects of important species (H, He, Na I, Mg II, Ca II, Ne I, and Fe II), global LTE conditions are assumed here for simplicity. We solve the EOS using a complete linearization scheme treating *all* considered species. Our method proved highly stable (even under extreme conditions of low temperature and high pressure), while being reliable and yet flexible to changes in elemental abundances and chemical composition. However, it is relatively slow on nonvectorizing computers. Therefore, we have compiled partial pressure tables which the model calculations may use. These tables extend over typical parameter ranges of

$$0.3 \leq \theta = 5040/T \leq 5.25\,, \quad \Delta\theta = 0.05\,;$$

$$-4.00 \leq \log P_g \leq 12.00\,, \quad \Delta \log P_g = 0.20\,;$$

for each mixture covered by our grid of model atmospheres.

The full composition of 334 species (listed in Table 1 for its most relevant section) was selected for the table construction so as to obtain accurate partial pressures for the species involved in opacity calculations. These include H_2, H_2O, CN, TiO, OH, CH, CO, VO, MgH, SiH, CaH, and FeH. The EOS tables are used *only* during the solution of the hydrostatic equation. Once this part of a model iteration is completed, the full EOS is solved with all species at all depth points in order to (*a*) check the accuracy of the solution and (*b*) ensure that the partial pressures of *all* species are known accurately at all depth points. The EOS tables are used, therefore, only to speed up the numerical calculations. We have calculated some of the models without using the EOS tables and found no significant change.

Our partition functions of atoms and ions are calculated internally by summing over the bound states taken from D. Mihalas (1993, private communication). The partition functions of most diatomic molecules are calculated according to the Tatum (1966) approximation. In the case of H_2 and CO, however, we opted for the more accurate polynomial expression by Irwin (1987). The partition functions of polyatomic molecules are also taken from Irwin (1988).

The dissociation constants of diatomic and polyatomic molecules are calculated internally by means of a Saha-like derivation (Tatum 1966). Atomization energies (energy relative to the neutral monoatomic reference species) are taken from the literature (e.g., CN with 7.77 eV from Costes, Naulin, & Dorthe 1990; FeH with 1.63 eV from Schultz & Armentrout 1991), and from the compilations by Irwin (1988), Huber & Herzberg (1979), and Rosen (1970).

The adiabatic gradient is calculated *analytically* including the most important species: H I–II, He I–II, H_2, CO, and electrons (as well as a number of species of secondary importance, for a total of 12 species), based on an algorithm developed by Wehrse (1977). Details of the numerical application of this algorithm may also be found in Allard (1990). This method has the advantage of high speed compared to numerical differentiation methods, while giving very accurate results. Additional species can be easily included if required by, for instance, a different mixture. The results of the adiabatic gradient calculations are in very good agreement with the results obtained through numerical differentiation of the entropy by Unsöld (1968) and by Wehrse (1974).

2.3. *Continuous Opacities*

The conventional continuous opacity sources included in our model calculations are H^- (John 1988), He^- and H_2^- (Vardya 1966), the H_2^+ and quasi-molecular hydrogen opacities (Carbon & Gingerich 1969; Gingerich 1971), C^- opacities (McDowell & Myerscough 1966). The most important *b–f* and *f–f* atomic processes (Hauschildt et al. 1994a; Allard 1994) are also included, based on cross sections compiled by Mathisen (1984).

However, under the atmospheric conditions involved in this study, molecular opacities dominate by several orders of magnitudes the conventional continuous opacities all across the entire spectrum. In the metal-rich regime, water vapor dominates the IR opacity. The H_2O absorption coefficients are therefore considered as a continuous opacity source in our models. We used for this purpose the Ludwig's (1971) tables of straight means opacities. This choice is motivated by the fact that the only available list of H_2O transitions, although describing the infrared bands well, fails to reproduce the continuum around 1.2 μm due to its increasing incompleteness toward J numbers greater than 30 (see also Allard et al. 1994a). The Ludwig data seem, on the other hand, to provide a satisfactorily description of the tip of the energy distribution (Allard 1994). The Ludwig data are valid for 300 K $\leq T_e \leq$ 3000 K.

© American Astronomical Society • Provided by the NASA Astrophysics Data System

1995ApJ...445..433A

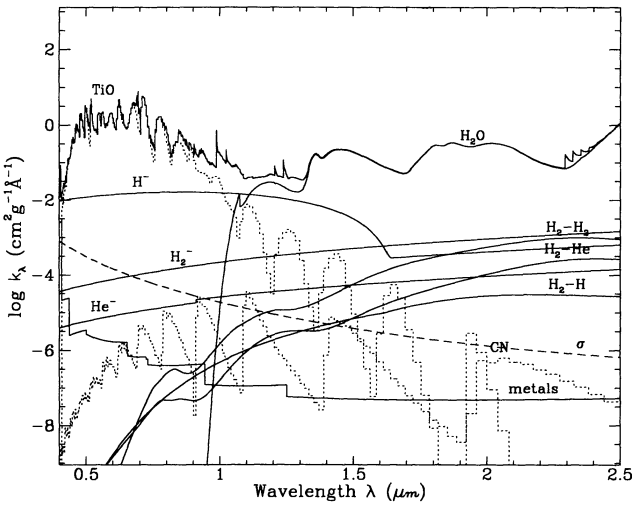

FIG. 1a

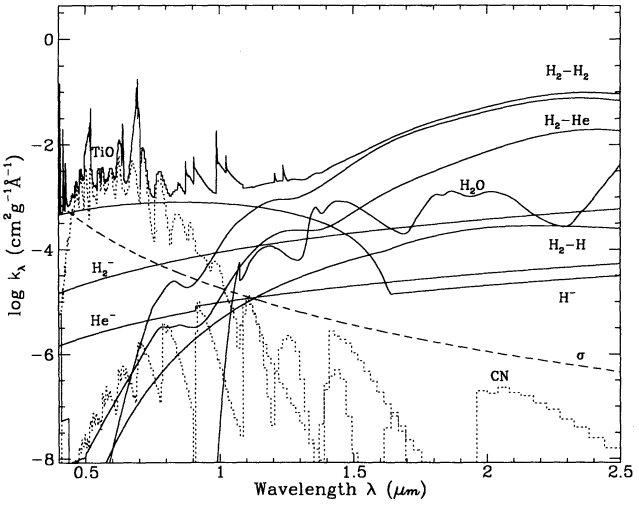

FIG. 1b

FIG. 1.—Molecular opacities dominate over the complete spectral range through which M dwarfs radiate the bulk of their emergent flux (~ 1 μm). In this figure, the topmost solid curve is the total opacity distribution included in the present model calculations. The opacity sources represented by full lines were used as "continuous"—opacities in the solution of the hydrostatic equation near $\lambda = 1.2$ μm. The dotted curves show some other important molecular absorbers (TiO, CN) included in the model spectra. The total scattering (Thomson + Rayleigh, H, H_2, He) is also shown as a dashed curve. (*a*) The situation at solar metallicity; (*b*) the corresponding situation in the low-metallicity regime for $T_{\rm eff} = 2800$ K, $\log g = 5.0$. Note how the CIA gradually replaces H_2O to form the IR continuum at low metallicities. The ~ 1 μm region is governed by VO and FeH opacities.

Since electronic temperatures within the model photospheres often exceed 3000 K, these SM opacity profiles have been conservatively extrapolated up to 4000 K (Allard 1994). In spectral ranges not covered by the Ludwig's tables ($\lambda < 1$ μm), we have adopted JOLA H_2O opacities (Tsuji 1966).

Similarly, in metal-poor regimes where pressure-induced H_2 opacities become the leading IR opacity source, we have included the collision-induced absorptions (CIA) (Borysow 1993, and references therein) of H_2–H_2, H_2–H, and H_2–He based on Lenzuni et al. (1991) as continuous opacity sources in our models.

Figure 1*a* and 1*b* show the resulting continuous opacity profiles for these two opacity limits, i.e., a solar and an extreme metal poor ($[M/H] = -2.5$) mixture, where the gas conditions are chosen to represent typical model conditions.

2.4. *Molecular Band Opacities*

As pointed out in the previous section, molecular band absorption is the primary source of blanketing in most spectral regions of M dwarf atmospheres. The millions of molecular transitions, however, often lack even approximate oscillator strengths, while the broadening mechanisms in the high gas pressure conditions encountered in M dwarf atmospheres are also rather poorly understood. This situation renders a line-by-line approach to the molecular opacities of M dwarfs far more complicated than in the case of extended M giant atmospheres. But precisely because of the higher pressure conditions, M dwarfs are presumed better suited to a statistical treatment of their molecular opacities. The band model techniques, for example, offer an interesting alternative for the dense atmospheres of cool dwarfs.

For this work we use Golden's (1967) formalism of the JOLA technique. For reversed bands we used also the more general JOLA formulation by Zeidler & Koester (1982). This technique allows us to approximate the absorption within a band with help of only a limited number of molecular constants: the rotational line structure in the bands is then reproduced by a continuum distribution. These molecular constants are generally taken from Huber & Herzberg (1979) or alternatively from Rosen (1970).

The applicability of this technique depends on the typical line spacing in each given molecular band; i.e., it assumes that the molecular lines overlap without being saturated (see also Tsuji 1994 for a review of the subject). Although the lines of some important molecules such as H_2O are expected to overlap, this is certainly not the case for several molecules of importance in cool dwarfs spectra (see Kui 1991). Therefore, we have used the JOLA approach only for molecular bands for which we lack all necessary line data.

For instance, the rotational analysis by Phillips et al. (1987) has allowed a major improvement to the model spectra of Allard (1994): the inclusion of FeH opacities. The most striking FeH feature is the Wing-Ford band, associated with the $\Delta v = 0$ transitions of the $F\,^4\Delta$–$X\,^4\Delta$ system of the molecule. Those FeH features are seen in all M dwarfs of spectral type later than M6, and their strengths are observed to increase significantly toward lower effective temperatures. This makes FeH an attractive parameter indicator for cool dwarfs and brown dwarfs candidates close to the stellar mass limit.

For the opacities of the TiO molecules, which define the visual and near-IR continuum in M dwarfs, we prefer the tabulated SM coefficients by Collins (1975). However, we had to resort to the JOLA approach for two of the TiO systems which were not included in Collins's original analysis: ϵ and ϕ.

Also included in the JOLA approach are the near-IR bands of CaH and VO. All other molecular absorbers are included in a line-by-line treatment as described in § 2.6 below. However, several bands of interest could not be included by lack of even the most elementary spectroscopic data needed to apply the JOLA (e.g., CaOH).

2.5. *Oscillator Strengths for JOLA Bands*

For explorers in the realm of molecular astrophysics, the most valuable—and rarest—treasures are accurate oscillator

© American Astronomical Society • Provided by the NASA Astrophysics Data System

1995ApJ...445..433A

TABLE 2

JOLA AND SM OPACITY DATA

Band	System	Technique/Source	f_{el} Source	f_{el}
TiO α	(C–X)	SM/Collins & Faÿ 1974	Davies et al. 1986	0.191
TiO β	(c–a)	SM/Collins 1975	Davies et al. 1986	0.278
TiO γ	(A–X)	SM/Collins & Faÿ 1974	Davies et al. 1986	0.163
TiO γ'	(B–X)	SM/Collins 1975	Davies et al. 1986	0.137
TiO δ	(b–a)	SM/Collins 1975	...	0.038[a]
TiO ϵ	(E–X)	JOLA/Golden 1967	...	0.048
TiO ϕ	(b–a)	JOLA/Golden 1967	Davies et al. 1986	0.012
VO	(A–X)	JOLA/Golden 1967	...	0.016
VO	(B–X)	JOLA/Golden 1967	...	0.280
VO	(C–X)	JOLA/Golden 1967	...	
CaH	(A–X)	JOLA/Zeidler & Koester 1982	...	0.350
CaH	(B–X)	JOLA/Zeidler & Koester 1982	...	0.120
FeH	(F–X) (0–0)	JOLA/Zeidler & Koester 1982	...	0.038
FeH	(F–X) (1–1)	JOLA/Zeidler & Koester 1982	...	0.010
FeH	(F–X) (0–1)	JOLA/Zeidler & Koester 1982	...	0.080
FeH	(F–X) (1–2)	JOLA/Zeidler & Koester 1982	...	0.025
FeH	(F–X) (1–0)	JOLA/Zeidler & Koester 1982	...	0.096
FeH	(F–X) (2–1)	JOLA/Zeidler & Koester 1982	...	0.200

[a] This slightly lower value than the Davis et al. measure of 0.048 yield better agreement with dMs spectra.

strengths for molecular bands. Under ideal circumstances, we prefer laboratory values when they exist, but in several cases we must resort to deriving "astrophysical" or empirical values. This is done iteratively by fitting the observed strengths of corresponding features observed in the spectra of an actual star.

Once the electronic band oscillator strength is available, we deduce the vibrational oscillator strengths for each subband and branch using the relation by Golden (1967):

$$f_{v'v''} = f_{el}\, q_{v'v''}\, \frac{\omega_{v'v''}}{\omega_0} .$$

The Franck-Condon factors $q_{v'v''}$, when unavailable, are calculated according to Nicholls (1981, 1982).

Among the bands considered in the JOLA approach, only TiO has laboratory band oscillator strengths. For these and all the bands included in the SM of Collins (1975) we use the values by Davis et al. (1986).

Astrophysical values are used for the oscillator strengths of the CaH, FeH, VO, and for the TiO ϵ systems which were not included in Collins's (1975) work. Allard (1994) already derived astrophysical oscillator strengths for many of the JOLA bands of the present work in a test model calculation based on the spectrum of the classical metal-rich M dwarf VB 10. These values were updated for the new conditions introduced in the present models by the inclusion of new line opacities. Also, although the most important bands of the FeH $F\Delta^4$–$X\Delta^4$ system were already included in the 1993 models, the low resolution of the observed spectrum of VB 10 prevented at that time the inclusion of the complex subband structure. The spectra did not resolve the subband structure, making it impossible to determine the repartitions of oscillator strengths at the subband structure level. In this work we include the subband structure, based on higher resolution spectra of VB 10 (H. R. A. Jones, private communication). The SM and JOLA opacity data and the adopted values of the electronic band oscillator strengths are summarized in Table 2.

Figure 2 presents the overall fit to the energy distribution of VB 10 obtained with this approach. Beside the apparent discrepancies in the IR (discussed below), the quality of this fit is a significant improvement which eliminates most of the problems reported by Kirkpatrick et al. (1993). We also verified that the strengths of the JOLA bands provide equally good fits to corresponding features observed in M dwarfs all along the Kirkpatrick et al. (1993) temperature sequence. This bolsters our confidence in using these values throughout the present grid.

2.6. *Line Lists and Line Treatment*

The PHOENIX line database includes at present close to 70 million transitions: ~42 million atomic and ionic lines, ~22 million diatomic molecular lines (Kurucz 1993a, b), and ~6.2 million H_2O (Miller et al. 1994). Among the molecular species

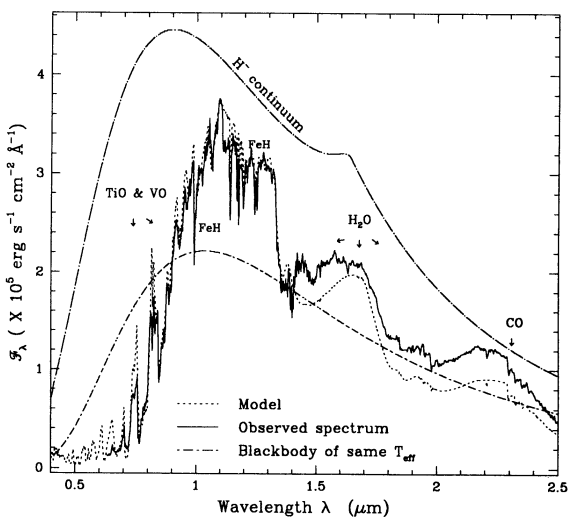

FIG. 2.—Our best fit to the spectrum of VB 10, based on the TiO and CO band strengths. (The derived atmospheric parameters are T_{eff} = 2800 K, log g = 5.0, assuming solar metallicity.) The observed spectrum is from Kirkpatrick et al. (1993) (0.6–0.9 μm) and Jones (private communication) (0.9–2.5 μm). Also shown are the corresponding H^- continuum, obtained by neglecting molecular opacities only in the radiative transfer, and a Planck distribution of same T_{eff}. Notice how the blackbody curve still underestimates the K-band flux (near 2.2 μm) even though it is depressed by the H_2O opacities.

© American Astronomical Society • Provided by the NASA Astrophysics Data System

1995ApJ...445..433A

represented in PHOENIX's database are H_2, CH, NH, OH, MgH, SiH, C_2, CN, CO, SiO, and their isotopes.

For this work, as mentioned earlier, we adopt the Ludwig straight mean opacities for water. Therefore, the H_2O line list is not included in the model grid calculations, but is used specifically for high-resolution IR spectroscopic studies (eg., Jones et al. 1995).

Not all of the line transitions need to be considered for every T, ρ point of an atmosphere. Therefore, before the calculation of the radiation field, a smaller subset is formed from the original lists. First, three representative points are chosen in the atmosphere. Then using the densities and temperatures for these points, the absorption coefficient in the line center, κ_l, is calculated for *every* line and compared to the corresponding continuum absorption coefficient, κ_c. A line is transferred to the "short list" if the ratio $\Gamma \equiv \kappa_l/\kappa_c$ is larger than a prespecified value of Γ (usually 10^{-4}) in at least one of the test points. In the subsequent calculations, all lines selected in this way are treated as individual lines; all others from the large line list are neglected. Using this selection process, we typically find that $\sim 5 \times 10^4$ (low T) to 2×10^6 (high T) metal lines, $\sim 6 \times 10^6$ molecular lines, and $\sim 2.1 \times 10^6$ H_2O lines (when used in place of the Ludwig data) are stronger than about 10^{-4} of the local continuum absorption (see Allard et al. 1994a).

We have tested this procedure by including *all* available molecular lines in a few models and found no significant differences in either the model structure or the emergent spectrum. However, we found that large values of Γ do *not* include a sufficient number of molecular lines; therefore, we use in all model calculations a value of $\Gamma = 10^{-4}$. A corresponding test of our line selection method for the atomic lines is given in Hauschildt et al. (1994a). We want to caution the reader that it is not clear how complete the line lists are for the conditions prevailing in M dwarf atmospheres. It is possible that many transitions—particularly in the infrared—may be missing from the lists and hence from our models.

For the calculation of the model atmospheres, we use a direct opacity sampling method on a fine wavelength grid with about 20,000 wavelength points (and not precalculated tables). A typical model calculation requires about 10 model iterations to reach an accuracy of better than 1% for both radiative equilibrium conditions [flux constancy and $\int \chi(S-J)d\lambda = 0$] in the layers that are in radiative equilibrium and temperature changes of less than 1 K in the convective layers. This is the case when only relatively poor initial estimates for the model structure are available; only three to five model iterations are required when we have better starting values. On an IBM RS/6000-580 workstation, the CPU time required for 10 model iterations is about 90 minutes and about 100 MB of main memory are required (mostly for the storage of the line lists). On a Cray C90 computer, the CPU times are typically reduced by factors of 5–10 depending on the model to be calculated.

PHOENIX includes various options for the treatment of line broadening. For the purpose of this model grid and low-resolution synthetic spectra, we use simple Gaussian profiles in order to save computer time. Calculations using full pressure broadening and Voigt profiles are typically a factor of 3–5 slower. For this reason, we include such a treatment only in the generation of the final high-resolution spectra, where care is taken to reiterate the models in cases where the model structure proves sensitive to the treatment of line profiles. The Voigt profiles include van der Waals interactions assuming that the collisional constants for the most numerous perturbers (i.e., H_2 and He I in M [sub]dwarfs atmospheres) do not differ significantly from their value for perturbations due to neutral hydrogen (Allard 1990). We prefer the van der Waals damping constant calculated from the classical Unsöld (1968) C_6 value, which we increment by $\Delta \log C_6 = 1.8$ as suggested by Wehrse & Liebert (1980), to the damping constants provided with the Kurucz list. Potential differences between the two approaches are being investigated and will be reported elsewhere.

A component of thermal Doppler broadening is also included which is often negligible in the line wings compared to pressure broadening, but dominates the line cores for the microturbulent velocities considered in our models ($\xi = 2$ km s^{-1}).

3. THE BASE MODEL GRID

Using the methods described in the previous section, we have computed a "base" grid of about 700 model atmospheres. The model grid currently covers a wide range of parameters encompassing the coolest known M Dwarfs, M subdwarfs, and brown dwarf candidates: $1500 \leq T_{\rm eff} \leq 4000$ K (with a typical stepsize of 100–500 K), $3.5 \leq \log g \leq 5.5$ ($\Delta \log g = 0.5$), and $-4.0 \leq [M/H] \leq +0.5$ ($\Delta[M/H] = 0.5$). The relative abundances of the isotopes of each element are assumed to be solar.

By "base" we mean here a grid calculated using opacity sampling for the atomic and molecular lines, but using SM opacities for the dominant absorbers (TiO and H_2O) and the JOLA technique for the remaining molecular opacities. We have several motivations and justifications for these assumptions. (i) This is an necessary and unavoidable first step to demonstrate that the SM and JOLA techniques are valid under the conditions prevailing in cool star atmospheres. (ii) The lists of molecular transitions of several important absorbers including H_2O (Allard et al. 1994a), if available at all, are still incomplete for the higher temperature conditions of dwarf star plasmas. (iii) The models can be used as starting point for a grid computed using a line-by-line treatment of the dominant opacities due to the TiO and H_2O lines (Allard & Hauschildt, in preparation).

We are currently extending and refining this grid as well as recalculating selected models with improved treatment of the molecular opacities. It is our intention to make the model structures plus the synthetic spectra available to the community. Because of the large number of combinations of input parameters for various synthetic spectra, we will not produce high-resolution synthetic spectra for large wavelength intervals; rather, we are prepared to calculate specific segments of specialized synthetic spectra upon request.

3.1. *The Structure of the Model Atmospheres*

In Figures 3 and 4 we display the structures of a small but representative subset of the model grid for a cool model ($T_{\rm eff} = 1600$ K) and four hotter models ($T_{\rm eff} \geq 2500$ K). Here we adopt two values of the metallicity—$[M/H] = 0$ (solar, *full curves*) and $[M/H] = -4$ (*dotted curves*)—and representative values of the surface gravity—$\log g = 3.5$, 4.0, 5.0, and 5.5 for $T_{\rm eff} = 1600$ K and $\log g = 4.0$, 5.0, and 5.5 for $T_{\rm eff} \geq 2500$ K. In general, the models with the smaller $\log g$ also have smaller pressures in the inner layers of their atmospheres. The structures of the other models are similar and are not shown here so as not to clutter the figures.

© American Astronomical Society • Provided by the NASA Astrophysics Data System

1995ApJ...445..433A

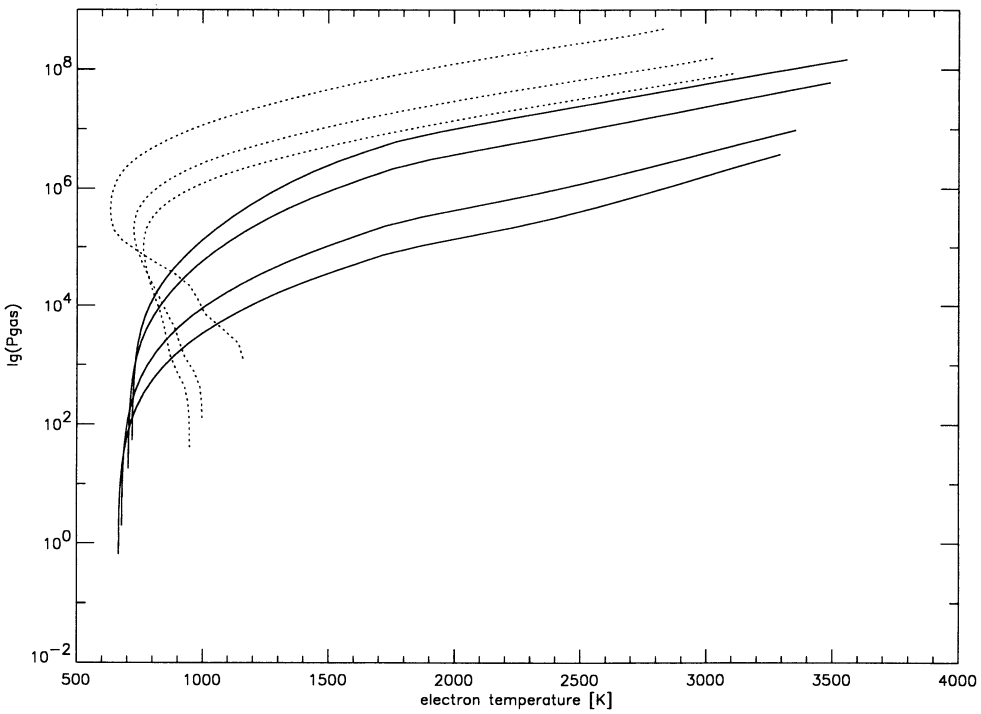

FIG. 3*a*

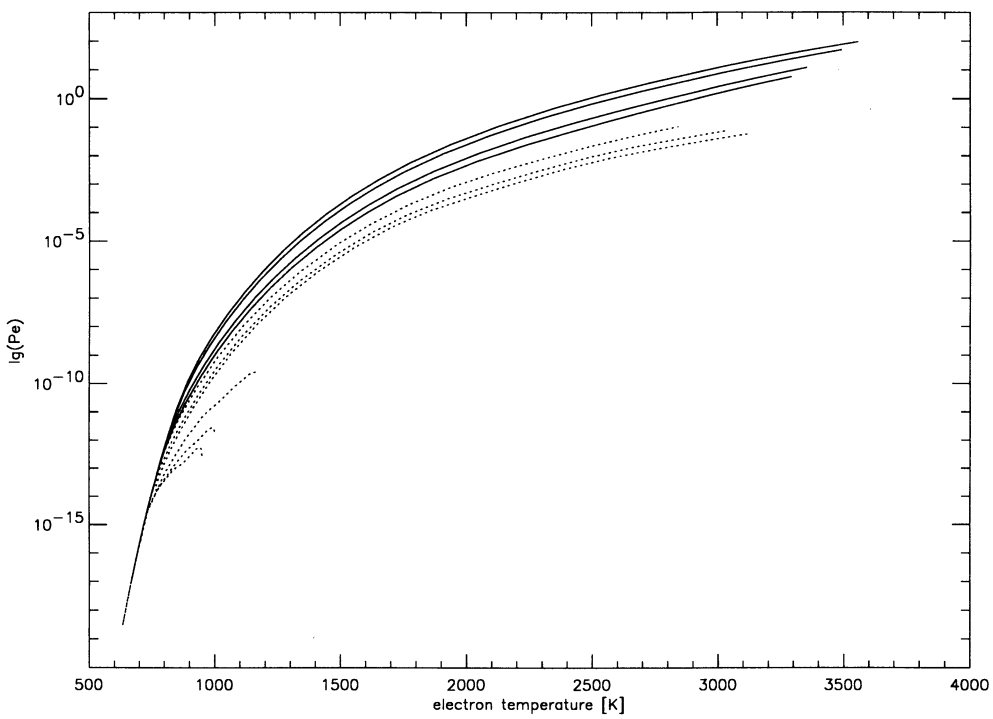

FIG. 3*b*

FIG. 3.—The structure of model atmospheres with $T_{\rm eff} = 1600$ K. (*a*) The run of the gas pressure P_g (in dyn cm^{-2}) vs. the electron temperature T_e; (*b*) the run of the electron pressure P_e (in dyn cm^{-2}) vs. T_e. The dotted lines are for models with $[M/H] = -4.0$; the full curves are for models with solar abundances, $[M/H] = -0.0$. We plot the structure for three values of log g, 4.0, 5.0, and 5.0 for both abundances sets. In addition, we show the results for log $g = 3.5$ for a model with solar abundances. The gravity decreases from the top to the bottom curve in each abundance set.

© American Astronomical Society • Provided by the NASA Astrophysics Data System

1995ApJ...445..433A

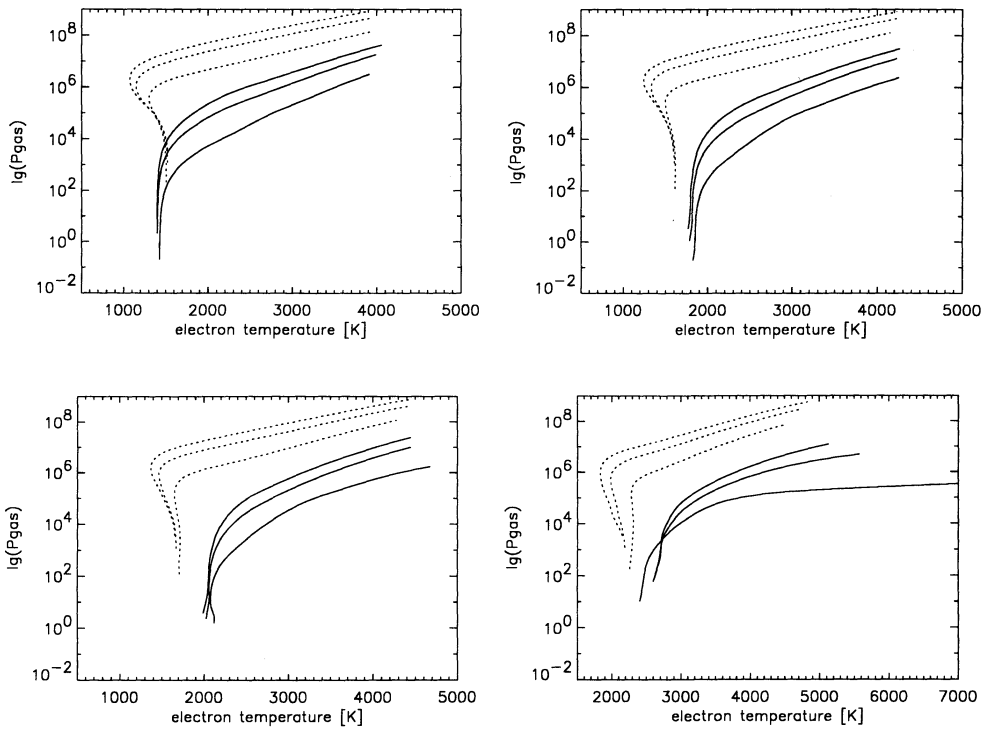

FIG. 4*a*

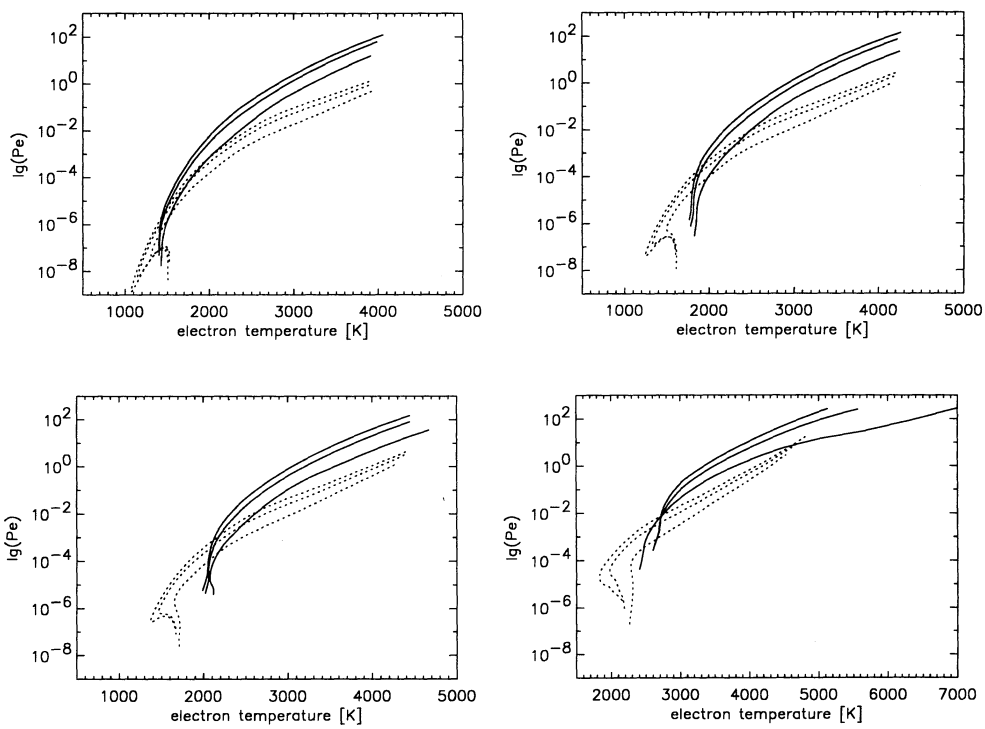

FIG. 4*b*

FIG. 4.—The structure of a small subset of the model atmospheres. (*a*) The run of the gas pressure P_g (in dyn cm^{-2}) vs. the electron temperature T_e; (*b*) the run of the electron pressure P_e (in dyn cm^{-2}) vs. T_e. The dotted lines are for models with $[M/H] = -4.0$; the full curves are for models with solar abundances, $[M/H] = -0.0$. We plot the structure for three values of log g, 4.0, 5.0, and 5.5 for both abundances sets. The gravity decreases from the top to the bottom curve in each abundance set.

© American Astronomical Society • Provided by the NASA Astrophysics Data System

1995ApJ...445..433A

The figures show that the lower metallicity models have much higher gas pressures than the models with solar abundances, but that the electron pressures of the low [M/H] models are significantly smaller. In addition, the lower metallicity models show a temperature inversion zone in the outer, optically thin ($\tau_{std} \leq 10^{-4}$) layers of the atmosphere. This is caused by an increase in the opacity induced by methane: Since the formation of methane (CH_4) is enhanced at the expense of CO due to the low-temperature and high-pressure conditions at lower metallicities, the resulting amount of free oxygen is bound in H_2O, TiO, and VO leading to a relative increase of the mean molecular opacity near $\tau_{std} = 10^{-4}$. This effect is not only seen at very low metallicity (as seen in Fig. 3) but is even observed at solar metallicity in very cool models ($T_{eff} \leq 2000$ K) of high gravity ($\log g \geq 6.0$); see Allard (1990).

The run of the electron pressure with temperature can be very complicated in the outer optically thin parts of the atmosphere due to the rapid change of the gas pressure with a comparatively slow change in the electron temperature, plus the presence of a temperature inversion zone. However, in the line-forming regions of the atmosphere, the run of P_e versus T_{eff} is usually very smooth. Particularly in the cooler models, we find that the electron pressures are greater than 6 dex smaller than the gas pressures and practically all of the electrons are supplied by the metals. Ionized molecules do not play an important role in the EOS or the formation of the spectrum for the models we consider here.

The effect of the gravity on the model structure is large, as expected. In particular, the structure of the hotter models ($T_{eff} \geq 3000$ K) with low gravity ($\log g \leq 4$) and close to solar abundances ([M/H] ≥ -0.5) is significantly different than the structure of the other models. An example is the $T_{eff} = 3500$ K, $\log g = 4.0$, [M/H] = 0.0 model shown in Figure 4. This model has much higher electron temperatures and lower pressures than the corresponding model for $\log g = 5.0$. This is caused by less-efficient convective energy transport in the $\log g = 4.0$ model as compared to the $\log g = 5.0$ model, which increases the temperature gradient.

3.2. *The Synthetic Spectra*

Figure 2 illustrates how molecular opacities dominate over the spectral range through which M dwarfs radiate the bulk of their emergent flux (~ 1 μm), leaving practically *no* window of true continuum. The H^- continuum lies more than 30% above the spectrum of the star, and the TiO absorption bands block more than 45% of the flux below 1 μm. The flux distributions are very different from the flux distributions of blackbodies of corresponding effective temperatures such that the blackbody distribution is a poor approximation, even redward of 2 μm.

In this figure, we have also plotted the observed energy distribution of the dM 8 star VB 10 for comparison. The model spectrum (*dotted line*) fits reasonably well the near-infrared spectrum and the depth of the CO bands near 2.3 μm, but fails to reproduce the water bands in the IR. It is not yet clear to what extent the flux calibration of the observed spectrum around 1.4 μm is responsible for part of this discrepancy. But a large share could possibly be attributed to shortcomings in the Ludwig H_2O opacities. Schryber, Miller, & Tennyson (1994) have recently compared the Ludwig opacities to other sources and found systematic errors in the former. In particular, they concluded that the Ludwig values overestimate the opacity of water by a factor of 2–3 in the 1–2 μm spectral range at the relevant temperatures for M dwarfs atmospheres. However, these conclusions are based on comparisons with other water opacity sources which are inadequate in this temperature range. The identification of the sources of error at play here and their solution await better water-line lists valid for high temperatures.

3.2.1. *Spectral Sensitivity to Effective Temperature*

The energy distributions of late-type dwarfs are very peculiar and in some ways, counter-intuitive. For example, the molecular opacities which globally define the continuum lock in place the peak wavelength at around 1.1 μm for solar metallicities. As T_{eff} decreases, the peak does not move redward as one would expect for a blackbody. This is shown in Figure 5 where the strong dependence of the TiO (optical) and water (IR) bands is clearly apparent. Therefore, although the stars do get redder, it is more due to a decrease in the visual flux than an increase in red. When looking for photometric bands most sensitive to very cool objects like brown dwarfs, it is vital to keep this in mind. The bandpasses where most of the flux escapes are (in order of decreasing importance) J, H, and K. Beyond the K band, the flux drops precipitously into a series of water bands growing in strength while the emergent flux decreases.

The dependence of the various spectral features on the effective temperature is demonstrated in Figure 6. These spectra have been folded with a Gaussian kernel to correspond to a resolution of 18 Å (the resolution of the observations by Kirkpatrick et al. 1993). We have plotted five models with $\log g = 5.0$ and solar abundances but with T_{eff} ranging from 4000 K (*full curve*) down to 2000 K (*dotted curve*).

The important bands of the CaH molecule near 6200 Å, 6400 Å, 6850 Å number among the most gravity-sensitive features of M dwarf spectra but are unfortunately completely blended with less sensitive TiO and VO features. The TiO bands and the CO first overtone are excellent T_{eff} indicators, and should therefore be used to estimate T_{eff} from observed spectra. The atomic lines typically get stronger and larger numbers of them succeed in piercing the molecular continuum with increasing effective temperatures. At the very low T_{eff}, only a few of the strongest resonance lines are still visible in the spectrum.

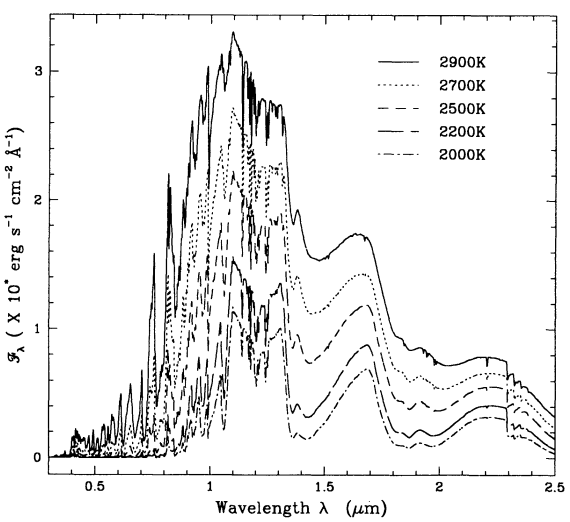

FIG. 5.—Low-resolution synthetic spectra for a model sequence with $\log g = 5.0$ and solar metallicity showing the behavior of the peak wavelengths toward the brown dwarf regime.

© American Astronomical Society • Provided by the NASA Astrophysics Data System

1995ApJ...445..433A

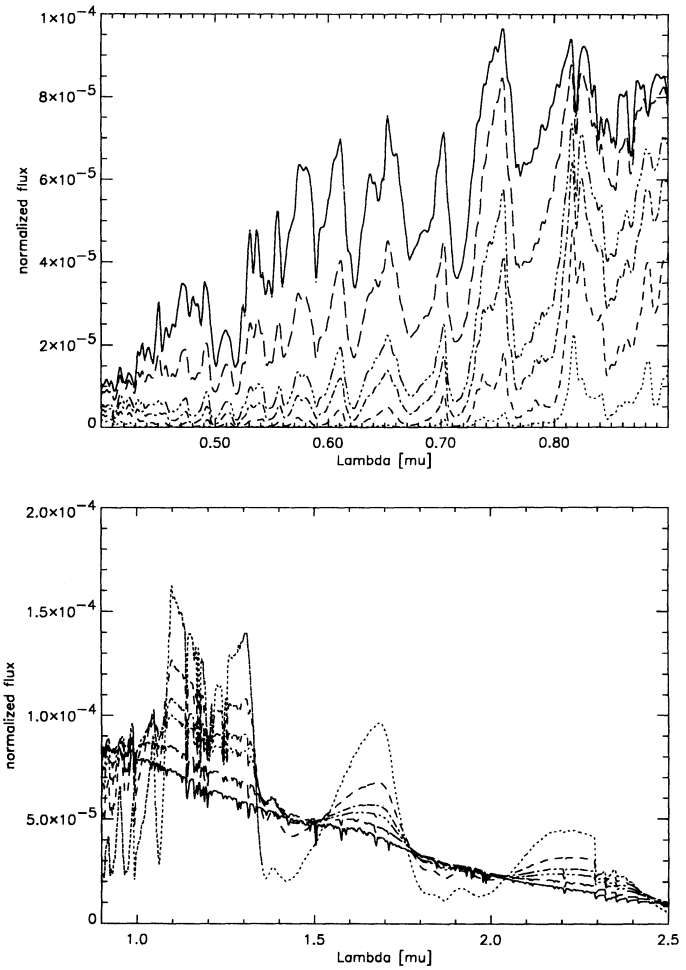

FIG. 6.—The low-resolution synthetic spectra for a model sequence with $[M/H] = 0.0$ and $\log g = 5.0$ for a number of effective temperatures. The synthetic spectra are plotted for five values of $T_{\rm eff}$, 4000 K (*full curve*), 3500 K (*long-dashed curve*), 3000 K (*dashed-triple-dotted curve*), 2800 K (*dashed-dotted curve*), 2500 K (*short-dashed curve*), and 2000 K (*dotted curve*). The spectra have been normalized to equal areas for clarity.

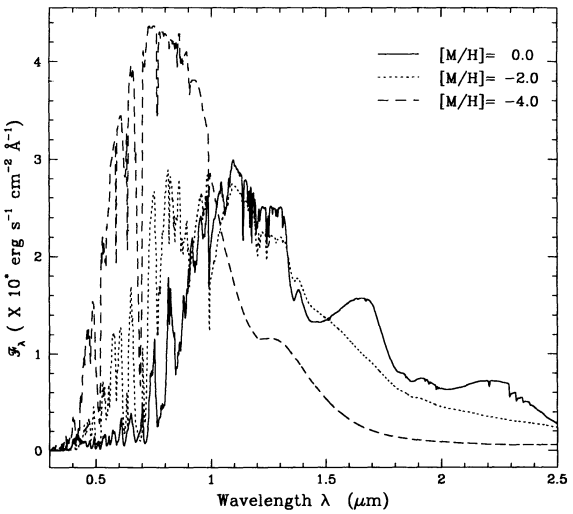

FIG. 7.—Low-resolution synthetic spectra for models of different metallicities corresponding roughly to the young disk ($[M/H] = 0.0$), halo ($[M/H] = -2.0$), and Population III ($[M/H] = -4.0$). The gravity is $\log g = 5.0$ for all models.

3.2.2. *Effects of Metallicity and Gravity on the Spectra*

In the coolest metal-poor objects, the CIA H_2 opacities, which are centered on 2 μm, further depress the continuum such that the flux emerges only in passbands *bluer* than H. This is depicted in Figure 7 where the IR flux distributions of three typical models are shown: one for metal-rich conditions expected in younger brown dwarfs bright enough to be seen; the others for halo and Population III stars. This figure shows clearly how the maximum of the energy distribution is progressively shifted to the *blue*. This is due to the progressive disappearance of the TiO molecule which dominates the opacity below 1.1 μm in the models of higher metallicities: the TiO absorption gives way to the H^- continuum and the radiation can escape from deeper, hence hotter, layers of the atmosphere. Moreover, a weakening of the H^- opacities themselves, owing to the rapidly decreasing availability of free electrons in the metal-poor regimes, enhances this effect. This combines with the growing wide CIA band opacities centered near 2 μm to dramatically increase the visual flux and at the same time decrease the IR flux. This change of the opacity as a function of wavelength also causes the effect—easily seen in the synthetic photometry presented below—that the metal-poor models actually appear bluer and hotter than metal-rich models.

Figure 8 shows the effects of the metallicity on the spectral features of the synthetic spectra with $T_{\rm eff} = 3000$ K and $\log g = 5.0$ in the optical (Fig. 8*a*) and the IR (Fig. 8*b*). The strength of the optical TiO and IR water and CO bands is reduced drastically, whereas the relative strength of the metal hydrides (preserved with higher probability than molecules involving metals only) increases. This is seen in particular in the bands of the MgH, CaH, and FeH molecules. This effect is also apparent in the strengths of atomic lines which also become stronger as metallicity decreases. This results from the increased gas pressures of metal-poor photospheres which compensate for the reduced number densities of atoms in the gas. With the exception of a few resonance transitions, most atomic lines finally disappear in the lowest metallicity models.

Figures 9*a*–9*c* show the gravity sensitivity of the synthetic spectra around the maximum of its energy distribution (0.9–1.4 μm) for the three representative metallicities. Since the issue of the gravity sensitivity of cool dwarfs energy distributions is particularly relevant to the search for spectral signatures of brown dwarfs, we have chosen sequences with $T_{\rm eff} = 1600$ K to illustrate the subject.

While the overall energy distributions of metal-rich models show little dependence on gravity, measurable effects are apparent in the relative strength of molecular bands: hydride bands (for reasons mentioned above) show a stronger pressure sensitivity than other metallic compounds. However, this is often masked by the simultaneous dependence of the band strength on the metallicity. Gravity effects can also be detected in the wings of strong atomic lines. Therefore, it seems more accurate to derive the gravity from line-width analyses rather than from low-resolution spectra.

The highly nonlinear coupling between the parameters $T_{\rm eff}$, $\log g$, and $[M/H]$ introduces the problem that changes in one of the parameters can be (at least partly) offset by changes in the other two parameters. For example, a change in $T_{\rm eff}$ can be partially simulated by a change in metallicity (higher $T_{\rm eff}$ corresponds roughly to lower $[M/H]$). However, this is true only at low resolutions; the potential ambiguity is removed by com-

© American Astronomical Society • Provided by the NASA Astrophysics Data System

1995ApJ...445..433A

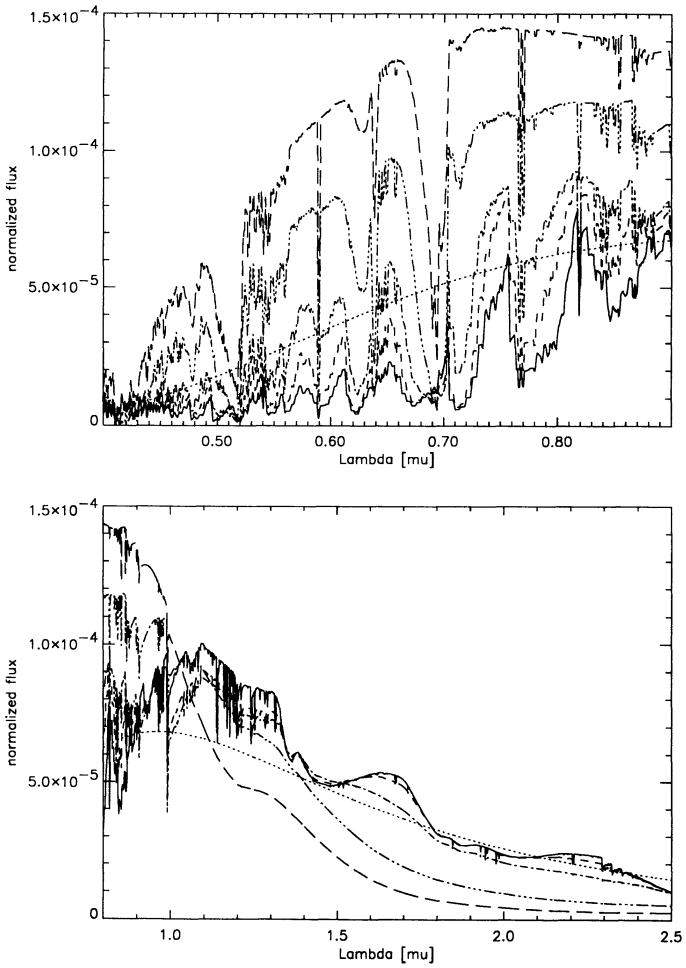

FIG. 8.—The low-resolution synthetic spectra for a model sequence with $T_{\rm eff} = 3000$ K and $\log g = 5.0$ around the maximum of the energy distribution. In each panel, we plot the synthetic spectra for five values of [M/H], 0.0 (solar abundances, *full curve*), −1.0 (*short-dashed curve*), −2.0 (*dash-dotted curve*), −3.0 (*dashed-double dotted curve*), and −4.0 (*long-dashed curve*). The dotted curve gives the blackbody energy distribution for $T = T_{\rm eff}$.

bining low-resolution with high-resolution spectra in some wavelength bands owing to the fact that line profiles react differently to changes of the parameters than the overall energy distribution. Therefore, a spectral analysis of M dwarfs should always use both low-resolution and high-resolution spectra in order to derive parameters with good accuracy.

We demonstrate this in Figure 10 by showing high-resolution infrared spectra between 1.14 and 1.24 μm for a number of different effective temperatures and gravities for solar abundances. We have chosen this particular range because high-resolution observations of M dwarfs are available and the synthetic spectra are currently being used to analyze these data (Jones 1995, in preparation). In each panel, the model with the highest $\log g$ also has the greatest line width. For the models with $T_{\rm eff} \leq 2000$ K, the gravity changes not only the line width but also strongly influences the strength of several FeH bands found in this spectral region. For higher $T_{\rm eff}$ the influence of molecular opacity is much smaller and at $T_{\rm eff} = 4000$ K, the spectrum is dominated by metal lines. The width of these lines is of course very gravity dependent and can be used to obtain the gravity from analyses of the observed spectra in this range.

3.2.3. *Spectral Signatures of Brown Dwarfs*

According to evolutionary models, M dwarfs and substellar objects can share similar atmospheric properties. Young brown dwarfs pass through a deuterium-burning-phase on their cooling tracks which heats the atmosphere through efficient convective mixing and mimics higher mass M dwarfs. A potential way to identify brown dwarfs unambiguously was proposed by Rebolo, Martin, & Magazzú (1992) and Magazzú, Rebolo, & Martin (1993): the detection of the Li I resonance doublet at 6780 Å. This method is based on the principle that the atmospheres of cool dwarfs are fully convective up to very low optical depths. Highly efficient mixing takes atomic lithium into the hot interior where is is destroyed *unless* the central temperature does not reach the Li-burning limit, which should be the case for brown dwarfs of $M < 0.06\ M_{\odot}$ according to interior models.

The formation of atomic lines like the Li doublet in atmospheres of cool dwarfs depends, beyond the abundance, on various factors: molecular binding, departures from LTE, treatment of convection and even feedback of chromospheric radiation. Pavlenko et al. (1994) have superficially investigated these effects using their spectral synthesis code (which is based on parts of ATLAS) combined with independent model structures (present work). To explore these factors with an atmospheric structure which adjusts self-consistently to the assumed conditions, we have conducted a separate analysis using our code PHOENIX. As a first step, we generated synthetic profiles of the Li doublet in a very cool model to look for molecular binding of Li assuming LTE. This is probably not a good assumption, even for $T_{\rm eff}$ as low as 1800 K; however, it can be used as a rough guideline for the formation of the doublet. (We are currently working on a non-LTE treatment for Li I.)

In Figure 11 we show synthetic line profiles of the Li I lines for a model with $T_{\rm eff} = 1800$ K, $\log g = 4.5$, and solar abundances (with the exception of lithium). We vary the lithium abundance from $\log \epsilon_{\rm Li} = 3.31$ (the meteoritic abundance of Li, *dashed curve* in Fig. 11) down to $\log \epsilon_{\rm Li} = 0.0$ (*top curve*). The dotted curve corresponds to solar Li abundance ($\log \epsilon_{\rm Li} = 1.16$). The differences in the profiles between the solar and meteoritic abundances are large, even in the line wings which are typically not very sensitive to non-LTE effects. This shows that the Li I lines can be used for low $T_{\rm eff}$ to distinguish brown dwarfs from M dwarfs, even though most of the Li nuclei are bound in molecules like LiCl. For more quantitative analyses of the Li abundance, non-LTE models must be used. A major problem with non-LTE calculations at such low electron temperatures are the collisional rates. Collisions with electrons are suppressed by the very low number density of electrons in the atmosphere; however, the collisional cross section of collisions between atoms and the most important species (H_2) are poorly known. Therefore, non-LTE line profile will depend sensitively on the particular assumptions of the collisional cross sections.

Significantly, none of the existing brown dwarf candidates could be confirmed by Marcy, Basri, & Graham (1994) and Martin, Rebolo, & Magazzú (1994), who set very low limits on the Li I doublet strength using new high-resolution, high-S/N spectra. Nevertheless, this does not rule out the existence of brown dwarfs, nor does it establish that the candidates are truly stellar since they could be simply transition objects just massive enough to destroy Li without ever reaching a state of stable hydrogen-burning. It is clear that other *independent* spectral signatures are needed. The next generation of models—incorporating line-by-line sampling of molecular

© American Astronomical Society • Provided by the NASA Astrophysics Data System

1995ApJ...445..433A

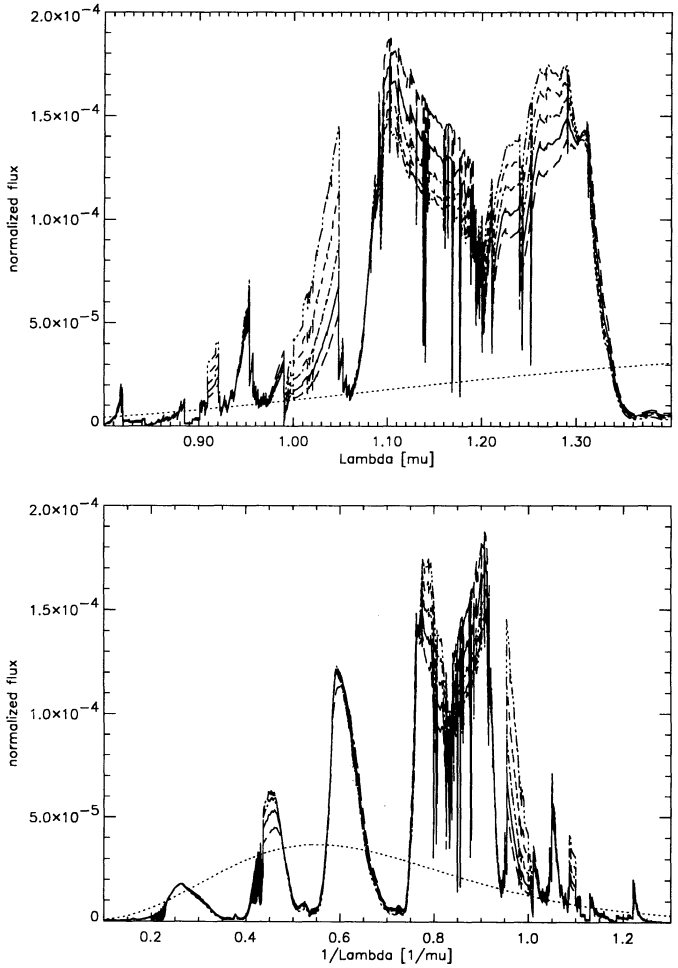

FIG. 9a

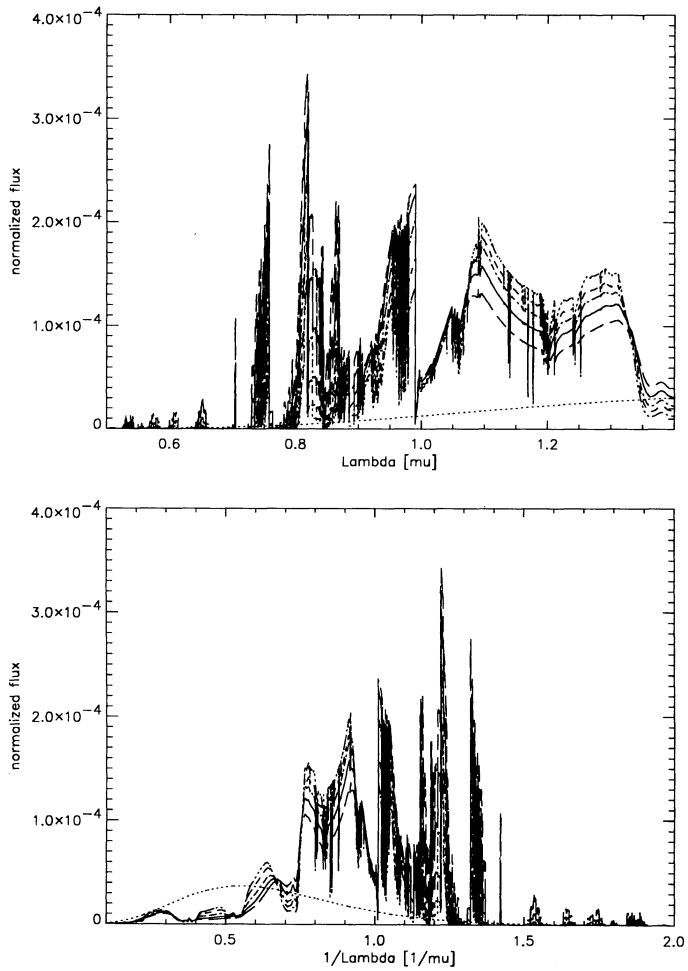

FIG. 9b

FIG. 9.—The low-resolution synthetic spectra around the maximum of its energy distribution (0.9–1.4 μm) for a model sequence with $T_{\rm eff}$ = 1600 K. (*a*)–(*c*) The spectra for models with metallicities of [*M*/H] = 0.0, −2.0, and −4.0, respectively. In each panel, we plot the synthetic spectra for five values of log *g*, 3.5 (*dashed-double dotted curve*), 4.0 (*short dashed curve*), 4.5 (*dash-dotted curve*), 5.0 (*full curve*), and 5.5 (*long dashed curve*). The dotted curve gives the blackbody energy distribution for T = 1600 K.

opacities—may also reveal global log *g* effects as yet unrecognized.

3.3. *Colors for M (Sub)Dwarfs*

3.3.1. *Synthetic Photometry*

In order to transform our synthetic spectra into photometric colors that are readily applicable to multicolor observations in the optical and infrared, we have computed synthetic *VRIJHKLL'M* magnitudes using our model spectra. The synthetic colors were computed by integrating the model fluxes over each bandpass. We adopted the following filter responses from the literature and other sources.

1. *V*, *R*, *I* (Cousin) system from Bessell (1990);
2. *J*, *H*, *K* CIT filters, accounting for atmospheric transmission (Persson, private communication). This system was originally defined by Elias et al. (1982) and is particularly relevant to the large *JHK* survey of M dwarfs by Leggett (1992). (*JHK* photometry on the Glass-Johnson system of filters described by Bessell & Brett 1988 has also been computed.);
3. *L*, *L'* (AAO), and *M*, as described by Bessell & Brett (1988).

To calibrate the flux-magnitude scale, we used the energy distribution of Vega as observed by Hayes (1985) and Hayes & Latham (1975) in the optical, and by Mountain et al. (1985) in the IR. Zero magnitudes (including *V*) and, correspondingly, zero color indices were assumed for Vega.

There is some debate about how to define the zero point of the magnitude scale: some people have used a sample of several A0 V stars to derive an "average" zero-mag definition; others have simply adopted Vega as the definition of zero at all wavelengths. We have adopted the latter approach and assumed V = 0 for Vega, even though the currently accepted value is V = +0.03. While this does not affect the synthetic colors, we caution that our absolute flux calibration may be somewhat uncertain.

Our zero-point magnitudes and fluxes are summarized in Table 3. These generally agree within 3% to corresponding values derived for the same filters by Bessell & Brett (1988) and Bessell (1990) (also shown in Table 3), even though they assumed *V* (Vega) = +0.03 and used a theoretical energy distribution for the star (Dreiling & Bell 1980). In fact, adopting the larger magnitude *and* theoretical fluxes is essentially equivalent to assuming *V* = 0 and adopting the slightly lower fluxes

© American Astronomical Society • Provided by the NASA Astrophysics Data System

1995ApJ...445..433A

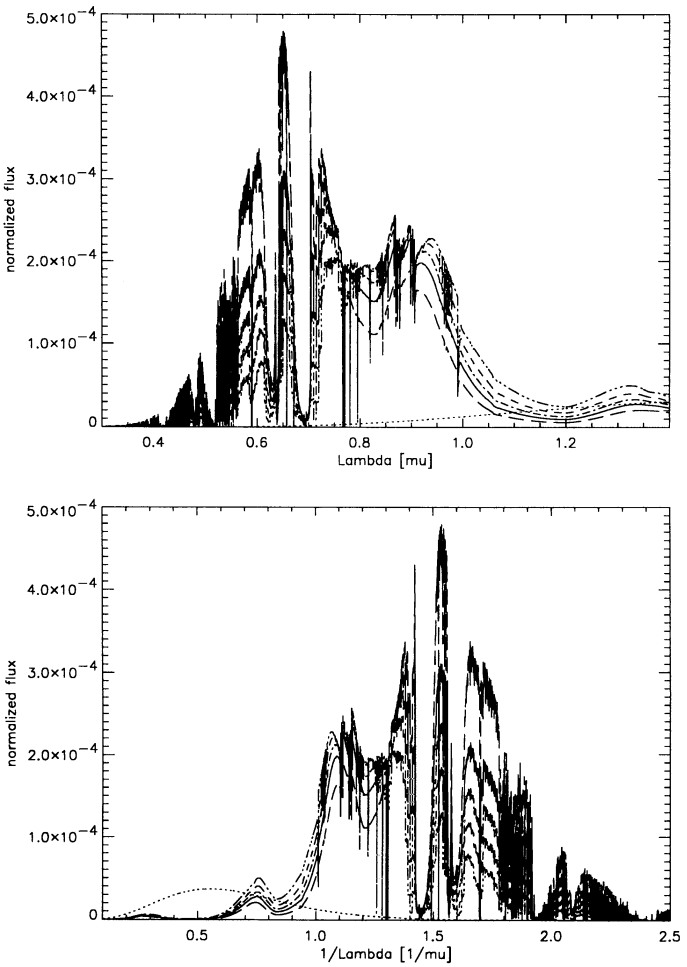

FIG. 9c

published by Hayes & Latham (1975). As a result, most of the differences between our approach and that of Bessell & Brett tend to cancel out. We also present in Table 3 the effective wavelength for each bandpass for both the observed spectrum of Vega (F_λ) and for a typical dM 8 star based on the best-fitting model of our grid to VB 10: $T_{\rm eff}$ = 2800 K, log g = 5.0, and [M/H] = 0.0. We show the resulting relation between different color indices and the effective temperature in Figures 12 and 13. In addition, we have calculated bolometric corrections for the V magnitude using the filter described above. For calibration, we have used a solar model atmosphere constructed with PHOENIX. The colors of our solar model agree within reasonable expectations with the observed colors so that this approach seems acceptable.

The tables giving photometric colors and bolometric corrections are not included in the paper in the interest of brevity, but are available in electronic form from the authors upon request.

3.3.2. *Comparison to Observations*

One of the largest homogeneous samples of optical-IR photometry of red dwarfs has been compiled by Leggett (1992), who obtained CIT photometry for a set of 322 stars. This provides an excellent basis of comparison for our synthetic colors, which we present in the form of color-color diagrams in Figures 12 and 13. In general, the agreement between the synthetic colors and the observations is good in various color-color planes; in fact, it is the best that has been achieved so far. Here we present only selected diagrams for the sake of brevity.

The $I-K$ versus $V-K$ diagram is a good metallicity discriminant for the coolest dwarfs. As metallicity decreases the models become decreasingly sensitive to $T_{\rm eff}$. When the metallicity reaches typical values for halo populations ([M/H] ≈ -2.0), $I-K$ is virtually insensitive to $T_{\rm eff}$. This results from a competition between the CIA opacities and the flux redistribution in the K band. Beyond the [M/H] ≈ -2.0 turning point, the CIA wins and drags the $I-K$ to bluer values with decreasing $T_{\rm eff}$. Note that the $T_{\rm eff}$ sequences shrink globally in both colors in Figure 12: while the metal-rich stars of Leggett's sample reach only temperatures as low as 2300 K, the presented metal-poor sequences can reach easily $T_{\rm eff}$ values of 1500 K within that window.

All curves meet at the hotter end of the sequence ($T_{\rm eff} > 3700$ K). This indicates the diminished impact of molecular opacities at those temperatures. There, the models appear to meet the observations perfectly. The models indicate that most of the stars in Leggett's sample have metallicities from solar to -1.0, which could in principle be consistent with their membership to the disk population as inferred from space motion analysis (Meusinger 1991; Carlberg et al. 1985). However, the relative

TABLE 3

EFFECTIVE WAVELENGTHS,[a] ZERO POINT FLUXES,[b] AND MAGNITUDES[c]

Parameter	V	R	I	J	H	K	L	L'	M
$\lambda_{\rm eff}$	0.544	0.641	0.798	1.221	1.631	2.153	3.452	3.802	4.754
$\lambda_{\rm eff}$[d]	0.562	0.700	0.820	1.230	1.639	2.202	3.477	3.811	4.751
F_λ	35.808	30.136	24.047	16.188	10.604	6.906	3.023	2.550	1.719
Zeropoint ZP	0.021	0.208	0.453	0.883	1.342	1.808	2.705	2.890	3.318
Bessell & Brett 1988									
Bessell 1990	0.008	0.193	0.443	0.902	1.369	1.884	2.772	2.966	3.421
CIT Values									
$\lambda_{\rm eff}$	...	...	...	1.251	1.623	2.203			
$\lambda_{\rm eff}$[d]	...	...	...	1.256	1.637	2.214			
F_λ	...	...	...	15.603	10.636	6.641			
Zeropoint ZP	...	...	...	0.923	1.339	1.850			

[a] Wavelengths in μm.
[b] F_λ is 10^{-10} ergs s^{-1} cm^{-2} Å^{-1}) for a 0.00 magnitude star in each adopted passband.
[c] Mag = $-2.5 \log (F_\lambda)$ − ZP + const.
[d] Based on the best fitting model to VB 10 ($T_{\rm eff}$ = 2800 K; log g = 5.0, solar composition).

© American Astronomical Society • Provided by the NASA Astrophysics Data System

© American Astronomical Society • Provided by the NASA Astrophysics Data System

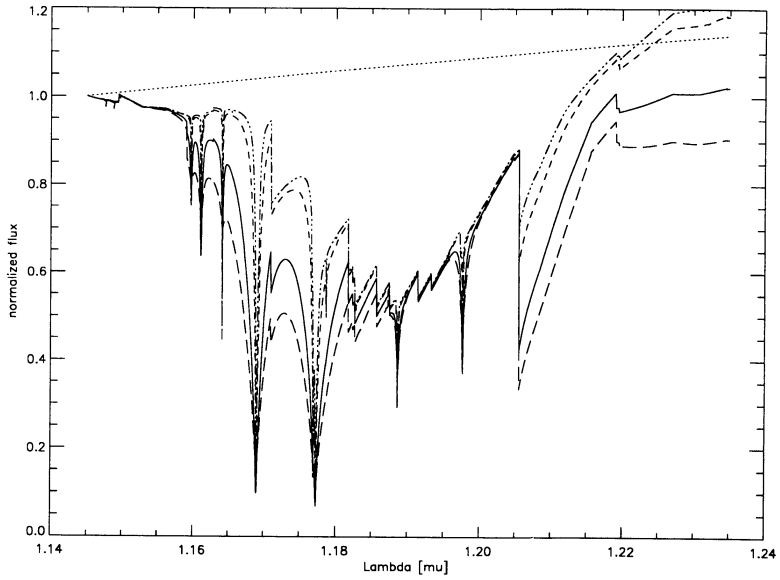

FIG. 10*a*

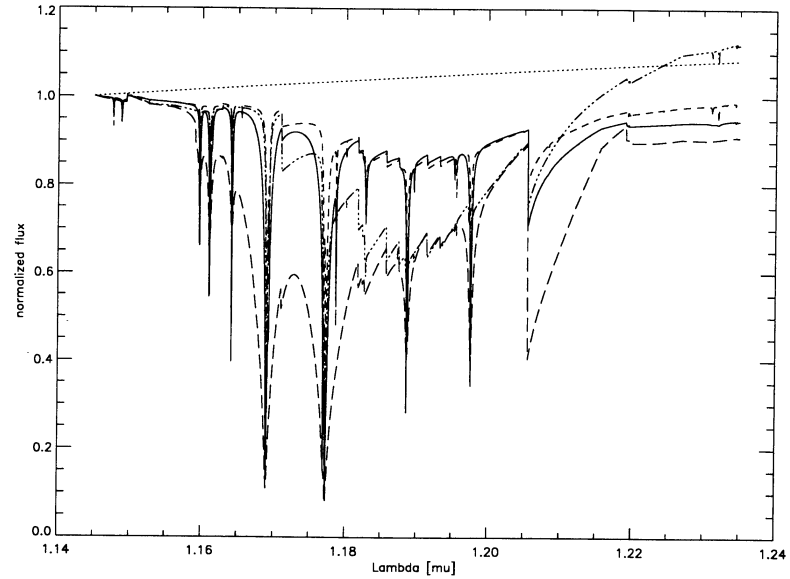

FIG. 10*b*

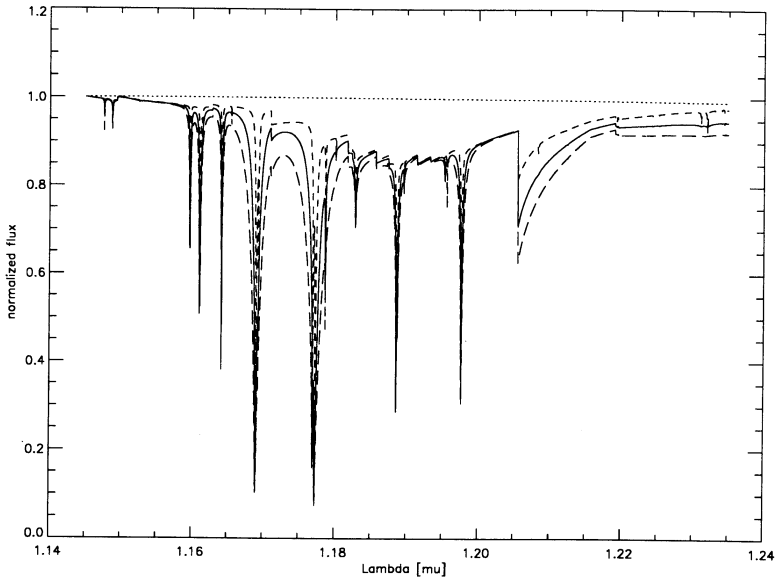

FIG. 10*c*

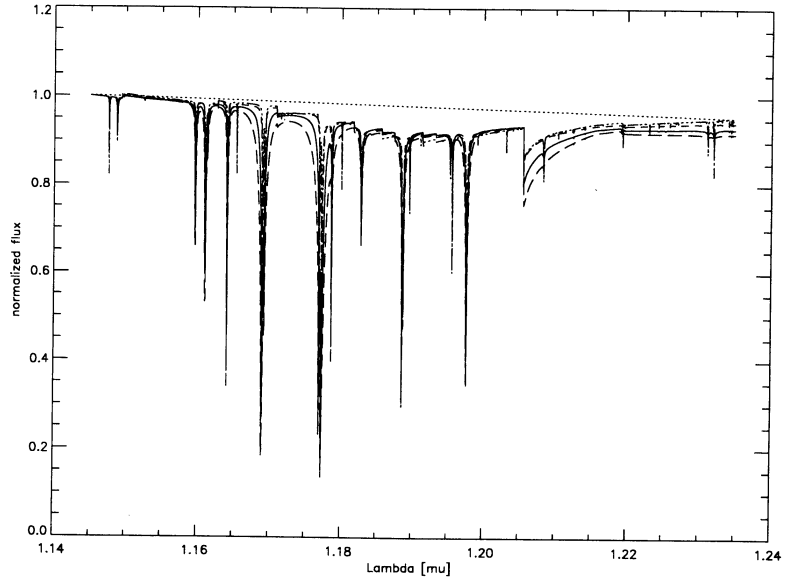

FIG. 10*d*

FIG. 10.—The high-resolution IR synthetic spectra from 1.14 μm to 1.24 μm for a model sequence with solar abundances (*a*)–(*e*) The spectra for models with effective temperatures of 1800, 2000, 2500, 2800, and 4000 K, respectively. In each panel, we plot the synthetic spectra for three values of log *g*, 3.5 (*dashed-double dotted curve*), 4.0 (*short dashed curve*), 4.5 (*dash-dotted curve*), 5.0 (*full curve*), and 5.5 (*long dashed curve*). The dotted curve gives the blackbody energy distribution for $T = T_{\rm eff}$.

1995ApJ...445..433A

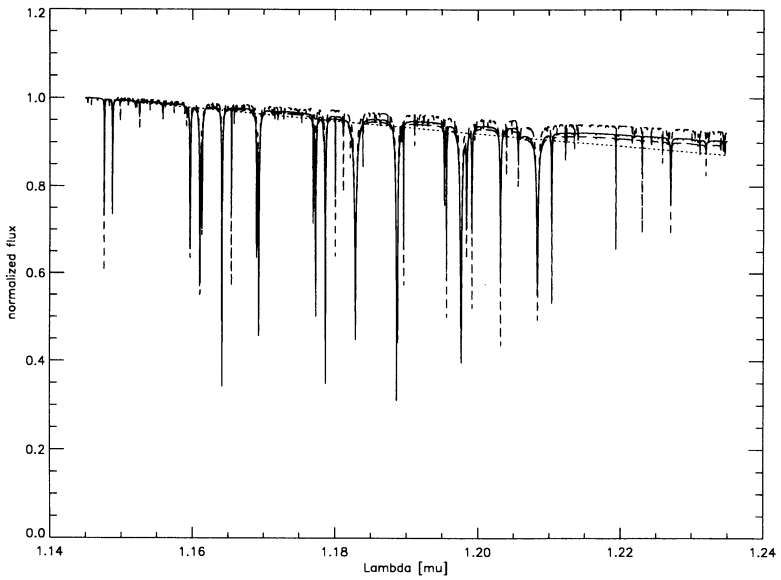

FIG. 10*e*

rarity of solar metallicity stars among the reddest part of the sample appears unnatural. We rather believe that this could be due to our use of the straight mean assumption for the main opacities: even lower metallicities toward the cooler regimes are required in order to compensate for an overestimation of the overall opacities in the models. This behavior resumes when saturation occurs in the molecular bands (here principally H_2O), as Figure 12 suggests for the reddest stars.

This problem is also apparent in the *JHK* diagram, where the models are systematically bluer in $J-H$ than the bulk of the observed colors by at least 0.1 mag. Here the situation is particularly complex. Although the stars are spread widely through this plane, the models suggest that interpretation of their atmosphere parameters based on *JHK* colors alone would not be straightforward. In Figure 13, we have reproduced the $T_{\rm eff}$ sequences for solar metallicity, a metallicity of

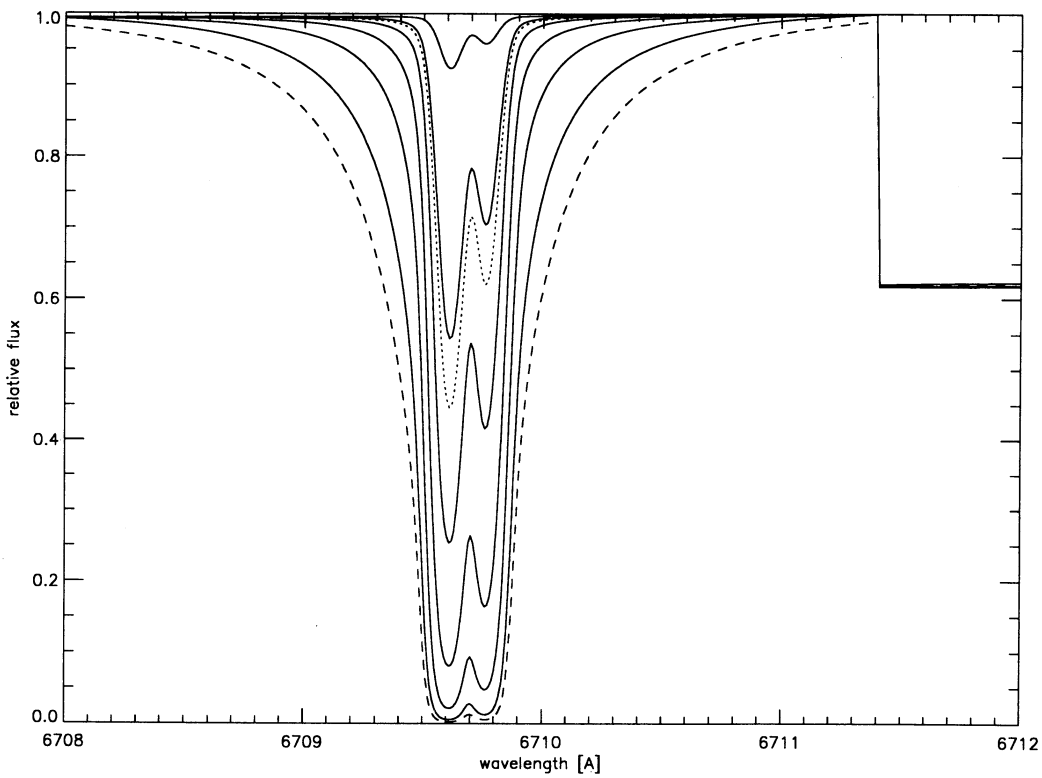

FIG. 11.—LTE synthetic Li I line profiles for a model with $T_{\rm eff}$ = 1800 K, log g = 4.5 and solar abundances (except Li). The dashed line gives the line profile for $\epsilon_{\rm Li}$ = 3.31 (meteoritic Li abundance), the dotted line the line profile for $\epsilon_{\rm Li}$ = 1.16 (solar photosphere Li abundance). The full curves give the line profiles for log $N_{\rm Li} \equiv \epsilon_{\rm Li}$ = 3.0, 2.5, 2.0, 1.5, 1.0, and 0.0 (*lower to upper curves*, respectively) relative to log $N_{\rm H}$ = 12 by number.

© American Astronomical Society • Provided by the NASA Astrophysics Data System

1995ApJ...445..433A

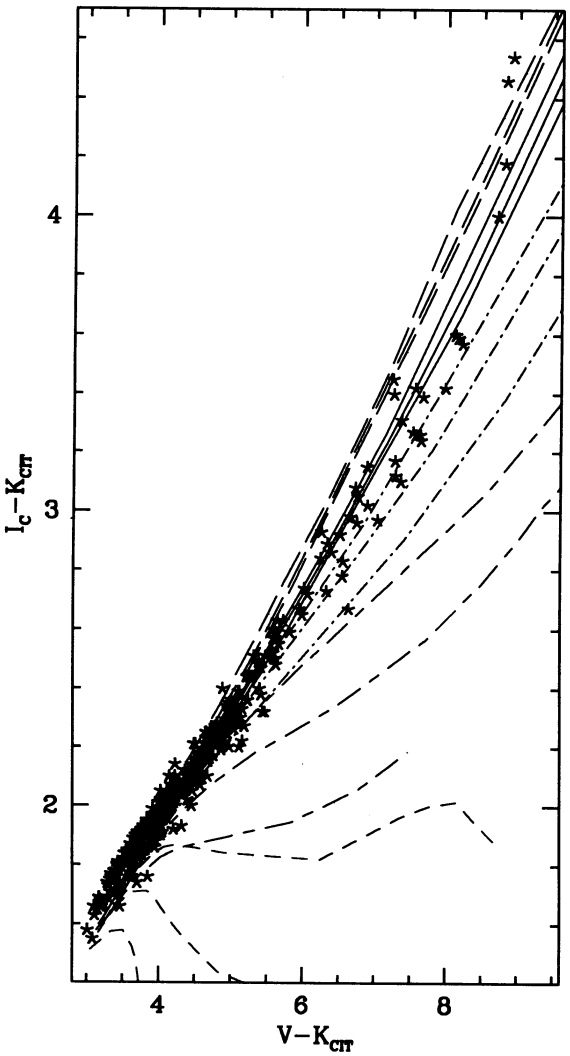

FIG. 12.—Synthetic color indices as function of the effective temperature for a range of metallicities and gravities: Solar (*long dashed curves*), [*M*/H] = −0.5 (*full lines*), [*M*/H] = −1.0 (*dot-dashed curves*), [*M*/H] = −1.5 (*short-dash long-dashed curves*), and [*M*/H] = −2.0 (*short dashed curves*). The values of gravity considered here are log g = 4.5 (*uppermost curve*), log g = 5.0 (*middle curve*), and log g = 5.5 (*lowest curve*) for each mixture. The observations of Leggett (1992) are represented by star symbols. The reddest stars in this diagram, LHS 2397a and LHS 2924, are found to be as cool as 2400 K and 2300 K, respectively, while the bulk of the sample coincides with models of $T_{\rm eff} \approx$ 3700 K if solar metallicity is assumed.

[*M*/H] = −0.5 and several metal-poor sequences. As can be seen, the metal-rich sequences curl around from the [blue $H-K$, red $J-H$] end (hot end) to the [red $H-K$, blue $J-H$] corner (cool end), crossing on the way to the lower portion of the diagram. This behavior reflects once again the struggle of the stars to release their fluxes as $T_{\rm eff}$ decreases: the growing IR molecular opacities efficiently redden the energy distribution until saturation in the water bands and redistribution effects finally stabilize the emergent fluxes in the water opacity troughs where the H and K bandpasses sit. If water opacities are overestimated, either due to the SM approximation or because of independent shortcomings of the Ludwig data, the consequences would be simply to exaggerate the amplitude of these loops in the metal-rich regime where water still dominates the IR energy distribution. These effects are clearly apparent in Figure 13. The increasing action of the CIA opacities is also seen in this *JHK* diagram. Here the CIA opacities cause the loops to curl back on themselves by [*M*/H] = −0.5. The halo population is expected to fall along nearly straight lines toward the blue end of this plane.

The discrepancies noted above are least apparent in color diagrams involving on both axes a red-IR color: both axes are then shifted blueward by a similar amount. As the TiO and H_2O opacities give way to continuous opacities toward the low-metallicity regime, the present models provide a better representation of low metallicities and halo stars. In order to resolve the remaining discrepancies, models with a full line-by-line treatment of the water and TiO opacity will be required.

4. CONCLUSIONS

In this paper we have described the results of our latest model atmospheres and synthetic spectra for M (sub)dwarfs,

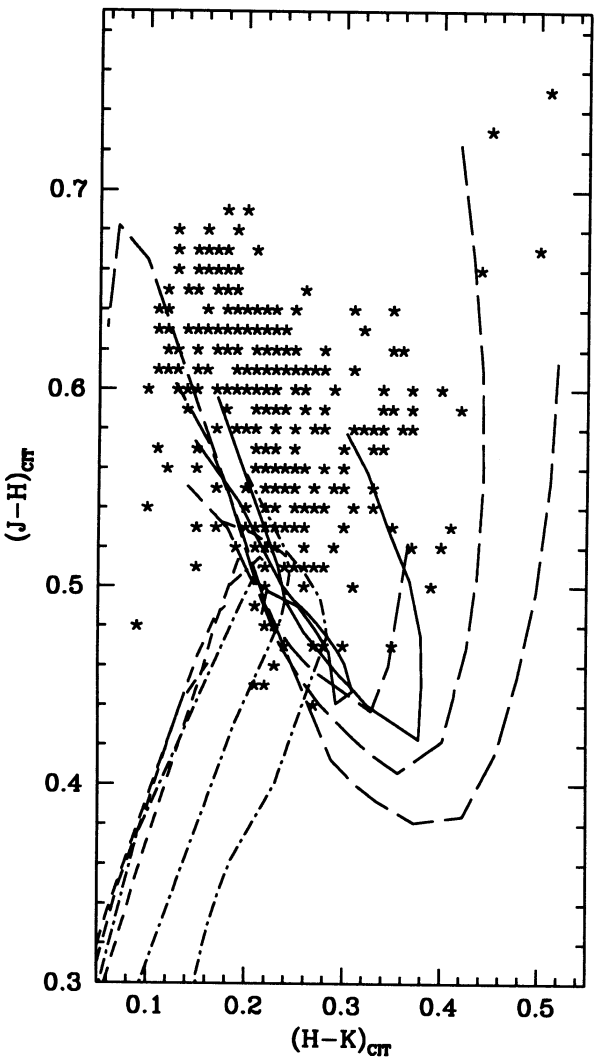

FIG. 13.—Same as Fig. 12, in the *JHK* color plane. Here only two values of the gravities (log g = 4.5 and 5.0) are shown for [*M*/H] = −0.5 to preserve the clarity of this diagram. The gravity increases from the outer curve to the inner curve for metal-rich mixtures. In the metal-poor regime, gravity increases and metallicity decreases toward bluer $H-K$ values. The hot portions of the sequences (> 3500 K) cross around $J-H$ = 0.5. The cool end extends, for the metal-rich models, toward the red portion of the diagram; for the metal-poor models, to the opposite blue portion of the diagram. The absence of stars in the latter section reflects the nearly solar metallicity of the Leggett sample.

© American Astronomical Society • Provided by the NASA Astrophysics Data System

1995ApJ...445..433A

based on straight mean opacities for the dominant molecular absorbers, i.e., H_2O and TiO. This new model grid constitutes a significant improvement over the earlier models by Allard (1990). We have introduced an opacity sampling treatment of atomic and molecular lines and included the FeH bands as well as several new molecular opacities.

We have computed an extensive "base model grid" of more than 700 cool dwarf atmospheres. Despite several discrepancies noted in the presented comparisons with observations, the new model spectra better define the basic properties of M (sub)dwarf radiation fields. The synthetic spectra demonstrate the influence of the metallicity and gravity on low-resolution spectra. While we found that gravity has a relatively small influence on the low-resolution spectra and the overall energy distribution, it has a significant effect on high-resolution line profiles and details of the band systems. However, the effects of the gravity become stronger with lower effective temperatures. The metallicity has, on the other hand, a large effect on both the low- and high-resolution spectra. We found that the parameters of an observed star are probably best determined by using a combination of low-resolution and high-resolution spectra in order to minimize ambiguity generated by the coupling between the three parameters $T_{\rm eff}$, $\log g$, and $[M/{\rm H}]$.

We have also computed synthetic colors for various bandpasses based on our low-resolution spectra. The synthetic colors agree now within reasonable expectations with observations. The color-color diagrams and spectra offer much-needed alternatives to blackbody fluxes for the classification of very low mass stars and the estimation of their stellar parameters.

One serious problem which our models face remains the predicted strength of the IR water band, which leads to unreliable predictions in the *JHK* color plane. This difficulty will not be resolved until new more appropriate H_2O opacities become available.

Other improvements to the models immediately suggest themselves. For example, we have neglected non-LTE effects. This may not be a good assumption for treating individual metal lines. The collisional rates could be quite small owing to the lack of free electrons and the relatively small rates for collisions with, e.g., H and H_2. We are currently working on an extension of our handling of collisional processes toward lower electron temperatures, which we hope may shed some light on the importance of these processes in cool dwarf atmospheres.

We have also neglected possible external radiation fields. These may be important for the chemistry of the upper photospheric layers in some instances where nonnegligible UV radiation is incident on the photosphere from, say, a hotter companion or its own chromosphere. In such cases, PHOENIX can actually allow self-consistently for the effects of external radiation fields on the model atmosphere and on the synthetic spectrum (see Baron et al. 1994). We intend to investigate these effects in subsequent work.

Finally, the incorporation of more complete and better molecular line lists (in particular for water and TiO) and of grain opacities remains the first priority in the development of cool dwarf model atmospheres. We are presently investigating the effects on the models of treating line opacities also for the dominant absorbers (Allard et al. 1994; Allard et al. 1995).

The present grid represents our foundation for future improvements. New grids are therefore expected to become available much more frequently in the future. Low-resolution synthetic spectra and selected high-resolution IR spectra are already available for each model atmosphere of this "base" grid. All results can be obtained in electronic form upon request to either of the authors.

We would like to give special thanks to H. Jones and S. Leggett for instructive discussions and for providing their observations in an electronic form. We thank the referee for very helpful comments on an earlier draft of this paper. We also want to thank S. Starrfield for his support and J. M. Matthews for careful reading of the paper. Some of the calculations presented in this paper were performed on the Cray C90 of the San Diego Supercomputer Center (SDSC); we thank them for a generous allocation of computer time.

This work was funded in part by grants to G. F. Fahlman and H. B. Richer from NSERC (Canada); and by a NASA LTSA grant to Arizona State University. The development of PHOENIX's opacity database is sponsored by a grant from the American Astronomical Society.

REFERENCES

Allard, F. 1990, Ph. D. thesis, Univ. Heidelberg
———. 1994, in IAU Colloq. 146, Molecular Opacities in the Stellar Environment, ed. P. Thejll & U. Jørgensen (Copenhagen; NORDITA) in press
Allard, F., Hauschildt, P. H., Miller, S., & Tennyson, J. 1994, ApJ, 426, L39
Allard, F., et al. 1995, in preparation
Anders, E., & Grevesse, N. 1989, Geochim. Cosmochim. Acta, 53, 197
Baron, E., Hauschildt, P. H., & Branch, D. 1994, ApJ, 426, 334
Bessell, M. S. 1990, PASP, 102, 1181
Bessell, M. S., & Brett, J. M. 1988, PASP, 100, 1134
Borysow, A. 1993, in Molecules in the Stellar Environment, ed. U. G. Jørgensen (Lecture Notes in Physics, 428) (Dordrecht: Springer), 209
Burrows, A., & Liebert, J. 1993, Rev. Mod. Phys., 65, 301
Carbon, D. F., & Gingerich, O. 1969, in Proc. Third Harvard-Smithsonian Conference on Stellar Atmospheres, Theory and Observation of Normal Stellar Atmospheres, ed. O. Gingerich (Cambridge: MIT Press), 377
Carlberg, R., Dawson, P., Hsu, T., & VandenBerg, D. 1985, ApJ, 294, 674
Collins, J. G. 1975, J. Phys. B, 1975, 304
Costes, M., Naulin, C., & Dorthe, G. 1990, A&A, 232, 270
Davis, S. P., Littleton, J. E., & Phillips, J. G. 1986, ApJ, 309, 449
Dreiling, L. A., & Bell, R. A. 1980, ApJ, 241, 736
Elias, J. H., Frogel, J. A., Matthews, K., & Neugebauer, G. 1982, AJ, 87, 1029
Gingerich, O. 1971, Solar Phys., 18, 347
Golden, S. A. 1967, J. Quant. Spectrosc. Rad. Transf., 7, 225
Hauschildt, P. H. 1991, Ph.D. thesis, Univ. Heidelberg
———. 1992, J. Quant. Spectrosc. Rad. Transf., 47, 433
———. 1993, J. Quant. Spectrosc. Rad. Transf., 50, 301
Hauschildt, P. H., Starrfield, S., Austin, S. J., Wagner, R. M., Shore, S. N., & Sonneborn, G. 1994a, ApJ, 422, 831
Hauschildt, P. H., Störzer, H., & Baron, E. 1994b, J. Quant. Spectrosc. Rad. Transf., 51, 875
Hayes, D. S. 1985, in IAU Symp. 111, Calibration of Fundamental Stellar Quantities, ed. D. S. Hayes, L. E. Pasinetti, & A. G. D. Phillip (Dordrecht: Reidel), 225
Hayes, D. S., & Latham, D. W. 1975, ApJ, 197, 593
Huber, K. P., & Herzberg, G. 1979, Constants of Diatomic Molecules (New York: Van Nostrand Reinholt)
Irwin, A. W. 1987, A&A, 182, 348
———. 1988, A&AS, 74, 145
John, T. L. 1988, A&A, 193, 189
Jones, A., et al. 1995, in preparation
Kirkpatrick, J. D., Kelly, D. M., Rieke, G. H., Liebert, J., Allard, F., & Wehrse, R. 1993, ApJ, 402, 643
Kui, R. 1991, Ph.D. thesis, National Univ. of Australia
Kurucz, R. L. 1993a, Atomic Data for Opacity Calculations, Kurucz CD-ROM No. 1
———. 1993b, Molecular Data for Opacity Calculations, Kurucz CD-ROM No. 15
Leggett, S. K. 1992, ApJS, 82, 351
Lenzuni, P., Chernoff, D. F., & Salpeter, E. E. 1991, A&AS, 76, 759
Ludwig, C. B. 1971, Appl. Opt., 10, 1057
Magazzú, A., Rebolo, R., & Martin, E. 1993, ApJ, 404, L17
Marcy, G., Basri, G., & Graham, J. 1994, ApJ, 428, L57

© American Astronomical Society • Provided by the NASA Astrophysics Data System

1995ApJ...445..433A

Martin, E., Rebolo, R., & Magazzú, A. 1994, ApJ, in press
Mathisen, R. 1984, Photo Cross Sections for Stellar Atmosphere Calculations—Compilation of References and Data (Inst. of Theoret. Astrophys. Univ. of Oslo, Pub. Ser. No. 1)
McDowell, M. R. C., & Myerscough, V. P. 1966, MNRAS, 132, 457
Meusinger, H. 1991, A&A, 245, 57
Miller, S., Tennyson, J., Jones, H. R. A., & Longmore, A. J. 1994, in IAU Colloq. 146, Molecular Opacities in the Stellar Environment, ed. P. Thejll & U. Jørgensen (Copenhagen: NORDITA), in press
Mould, J. R. 1976, ApJ, 210, 402
Mountain, C. M., Leggett, S. K., Selby, M. J., Blackwell, D. E., & Petford, A. D. 1985, A&A, 151, 399
Nicholls, R. 1982, J. Quant. Spectrosc. Rad. Transf., 28, 481
Nicholls, R. W. 1981, ApJS, 47, 279
Pavlenko, Y., Rebolo, R., Martin, E., & García López, R. 1994, A&A, in press
Phillips, J., Davis, S., Lindgren, B., & Balfour, W. 1987, ApJS, 65, 721
Rebolo, R., Martin, E., & Magazzú, A. 1992, ApJ, 389, L83
Rosen, B. 1970, Tables Internationales de Constantes Selectionnees. 17. Donnees Spectroscopiques Relatives aux Molecules Diatomiques (New York: Pergamon)
Schryber, H., Miller, S., & Tennyson, J. 1994, J. Quant. Spectrosc. Rad. Transf., in press
Schultz, R., & Armentrout, P. 1991, J. Chem. Phys., 94, 2262
Tatum, J. B. 1966, Publ. Dom. Astrophys. Obs. 13, No. 1
Tsuji, T. 1966, PASJ, 18, 127
———. 1994, in IAU Colloq. 146, Molecular Opacities in the Stellar Environment, ed. P. Thejll & U. Jørgensen (Copenhagen: NORDITA), in press
Unsöld, A. 1968, Physik der Sternatmosphären (2d. ed. Heidelberg: Springer-Verlag)
Vardya, M. S. 1966, MNRAS, 134, 347
Wehrse, R. 1974, A&A, 35, 157
———. 1977, A&A, 59, 283
Wehrse, R., & Liebert, J. 1980, A&A, 86, 139
Zeidler, K. T. E.-M., & Koester, D. 1982, A&A, 113, 173

© American Astronomical Society • Provided by the NASA Astrophysics Data System